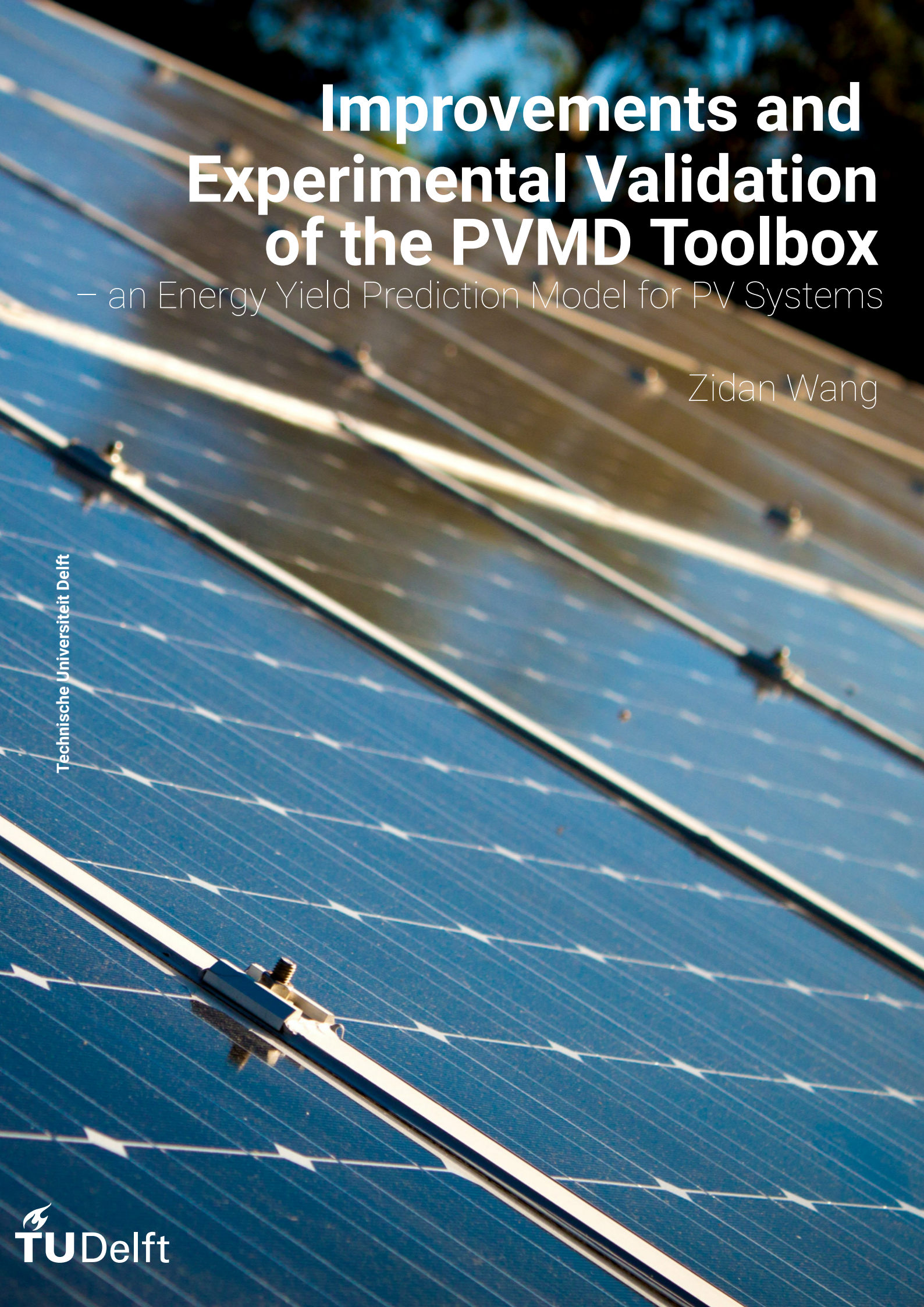

Improvements and Experimental Validation of the PVMD Toolbox

– an Energy Yield Prediction Model for PV Systems

Zidan Wang

Technische Universiteit Delft

TU Delft

Improvements and Experimental Validation of the PVMD Toolbox

– an Energy Yield Prediction Model for PV Systems

by

Zidan Wang

to obtain the degree of Master of Science
at the Delft University of Technology,
to be defended publicly on Friday June 28, 2019 at 9:30 AM.

Student number:	4708911	
Project duration:	September 10, 2018 – June 28, 2019	
Thesis committee:	Dr. O. Isabella,	TU Delft, supervisor
	Dr. R. Santbergen,	TU Delft, daily supervisor
	Dr. R. A. C. M. M. van Swaaij,	TU Delft
	Dr. Z. Qin,	TU Delft

An electronic version of this thesis is available at `http://repository.tudelft.nl/`.

TU Delft

Abstract

Photovoltaic (PV) system yield prediction models are an important topic in the field of PV solar energy. An accurate prediction model could not only be used for optimising the PV system design, but is also expected to realise the yield potential of innovative PV technologies. In the next generation of PV technologies, one of the most promising concept is the tandem solar cells. In the recent years, these cells have impressed the solar industry by their rapid growth of the maximum power conversion efficiency (PCE). Since tandem solar cells are still at the lab phase, their yield potential under realistic conditions are an interesting field of study as well.

However, the existing yield prediction models, such as PVSyst and System Advisor Model (SAM) are not yet available for these tandem cells. In order to fill this gap, a prediction model developed in the Photovoltaic Materials and Devices (PVMD) group of TU Delft, called the PVMD Toolbox, has been adapted to be compatible with the tandem solar cells.

In this thesis project, a version 3 of the Toolbox was developed. First the PVMD Toolbox was improved. Except monofacial c-Si cells and bifacial c-Si cell, it is now also available for tandem cells. One of the most promising tandem concepts, the perovskite/c-Si tandem, was taken as a reference tandem configuration integrated in the Toolbox. The Toolbox was also modified to take the influence of solar spectra into consideration and analyses cell performances individually. Secondly, the accuracy of the Toolbox was validated. A new figure of merit called 'relative total deviation' is put forward in this report, which calculates the ratio between the sum of deviations that each simulation introduces, and the total measured energy yield. When the electrical parameters were taken from the own measurements, the relative total deviation of simulation results was only 8.6 %. Finally, the Toolbox was applied to two case studies. In the first study, it was found that the annual energy yield (AEY) of perovskite tandems can be increased up to 0.4 % by optimising perovskite thickness for a certain location. The second case study compared the AEY of the tandem module and conventional c-Si module. Perovskite tandem module showed a high AEY, around 36 % higher than that of c-Si module. However, perovskite tandem had a lower specific yield as they are more sensitive to the spectral variation.

Preface

This thesis is a part of the final work of my 2-year student life in TU Delft. The last 2 years have been a challenging trip but yet full of excitement and joy. I am appreciated that I've learnt a lot during this journey and I am thankful to people I met here.

I would like to thank my daily supervisor Dr. Rudi Santbergen. Your knowledge and advice are much appreciated as they have helped me so much during this journey. I would also like to thank Dr. Olindo Isabella for giving me this opportunity to join this interesting project and also to be a part of the PVMD group. Thanks and appreciation are also to Dr. Rene van Swaaij and Dr. Zian Qin for being part of my thesis committee. I would want to express my gratitude to Prof. dr. Miro Zeman and Prof. dr. Arno Smets for sharing with us your knowledge in the PV courses. I am thankful to Andres, Juan Camilo, Hesan, Julen, Martijn and Eliora for your help during this journey. I am also thankful to everyone in the PVMD group for always being willing to help and share your brilliant ideas with me.

I would like to thank my office mates Anjali, Sukanya, Leo and Emilio. I really enjoyed the time being with you and thank you for always being helpful. Thanks to Carlotta, Ignacio and Thanasis, for discussing about the Toolbox with me.

I would also like to thank Yiran, Yifeng, Peiqing, Zhimin, Yue, Rong, Wanting and all the wonderful people I met in the Netherlands. Thank you for your help and support.

Finally I would like to express my gratitude to my parents, who always love me, support me and encourage me to break the comfort zone. 我爱你们!

Zidan Wang
Delft, June 2019

Contents

List of Figures

1 Introduction

This chapter introduces the background information required by the subsequent analyses. First, a review of photovoltaic (PV) system prediction models is given in Section 1.1. Secondly, in Section 1.2 an introduction to another research topic, the tandem cells, is given. Later a prediction model developed in TU Delft, called the Toolbox, is described in terms of its structures and limitations in Section 1.3. Based on the theoretical knowledge, the research question and goals are described in Section 1.4, followed by a brief description of thesis outline in Section 1.5.

1.1. Review of PV System Yield Prediction Models

The goal of this section is to briefly introduce the background knowledge of photovoltaic technology and the relevance of performance modelling of photovoltaic systems.

1.1.1. Background

The exhaustion of conventional sources, our deteriorating environment and the fast-growing energy demand have driven people to search for clean and plentiful energy sources. Renewable energies like that of the sun, wind, geothermal sources, biomass and tidal energy are used in electricity generation to support the daily lives of humans. Of all the requested sources, solar energy is regarded as one of the most secure, reliable and abundant energy source.

Even though human beings have made use of the solar energy and heat from the sun for heating and agriculture along with the development of mankind, the study on other solar energy technologies like photovoltaic technology, solar heating and solar thermal electricity has only been continuing for decades[1]. Since the first silicon solar cell patented in 1946[2, 3], power conversion efficiency (PCE) of silicon cells has increased from less than 1 % in 1946 to 26.7±0.5 % in 2017 as reported by Yoshikawa et al[4]. During the development of PV technologies, the installed PV capacity has gained an exponential increase as well, as shown in Figure 1.1[5].

A reason of this exponential growth is that since the beginning of this century, many countries have launched feed-in tariff schemes, which have encouraged the installations of PV systems. Another reason lies in the fact that cost of solar has reduced significantly, compared to conventional energy sources like coal as well as clean energy sources like wind energy, and is continuing to reduce, as shown in Figure 1.2. As recently as 2018 the annual PV installed capacity broke the threshold of 100 GW[5]. As a result, the accumulative total installed capacity reached 509.3 GW, while this value was 407 GW in 2017, 306.5 GW in 2016 and 229.9 GW in 2015[5]. Therefore it is concluded that there

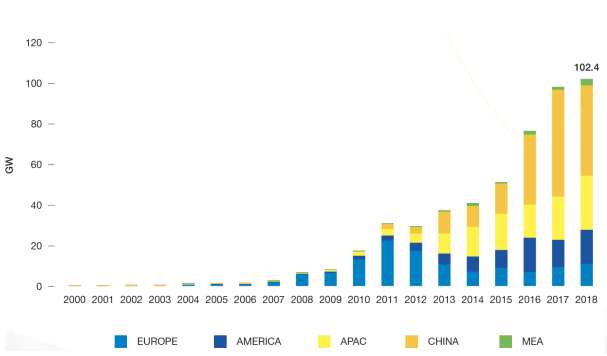

Figure 1.1. Global total PV installed capacity 2000 - 2018[5]

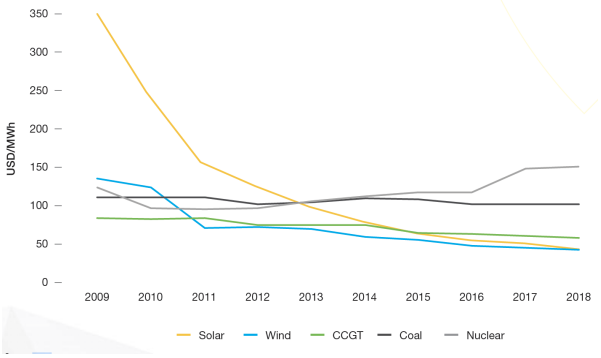

Figure 1.2. Electricity generation cost of solar energy, compared to other forms of power[5].

is an accumulating interest towards photovoltaic technologies.

1.1.2. PV System Yield Prediction Models

Although solar energy has gained a large installed capacity, its performance under realistic conditions is affected by irradiance, temperature and other weather conditions and could also suffer from electrical losses. In order to simulate the energy yield of PV systems and improve their designs, energy yield prediction models are necessary. Besides conventional solar modules, novel solar technologies, with new cell layer materials or innovative cell structures, have also attracted attention by showing a high cell efficiency or other interesting new features under standard test conditions (STC). However, these novel photovoltaic devices are still in the lab phase so that their energy yields and cell efficiency under realistic climate conditions are not available to measure. Therefore, it is also of interest to predict energy yields for these photovoltaic technologies. According to the annual energy yields (AEY) predicted based on realistic meteorological data, researchers can gain a direct insight into the energy yield potential of these innovative solar technologies under real-life conditions. Therefore, PV system energy yield prediction models could not only help improve conventional PV system designs, but is also useful for the research of new PV technologies.

There are several energy yield prediction models developed by some research institutes, which predict PV system energy yields based on the PV system designs and weather conditions but using different algorithms. These prediction models are mostly commercially available and some examples of them are introduced below.

PVsyst, developed by Swiss physicist Andre Mermoud and electrical engineer Michel Villoz, is one of the most popular prediction models. This model is designed for engineers, architects, researchers and students and combines prefeasibility, sizing and simulation tools for PV systems[6]. It provides users with a product data base to choose their interested solar module and other necessary components in a PV system and asks users to define their PV system design. For this customised PV system, energy yields are simulated, based on weather data taken from the Meteonorm software. Latitude and longitude resolutions can be as small as 0.5° in PVSyst Software[7], leading to a high accuracy of the prediction results. The predicted energy yield, along with some indicators of PV system performance such as performance ratio (PR) and specific energy, are given via simulations[6]. A disadvantage of this software is that available solar modules in the product data base are mainly conventional silicon solar modules, thus it could not simulate energy yields of innovative solar cell designs, such as tandem cells. In addition, it is not possible to study a PV system with reflectors in

PVSyst.

The **System Advisor Model (SAM)** is another widespread system energy yield prediction tool, developed by the U.S. Department of Energy and National Renewable Energy Laboratory (NREL). It provides project designers and managers, financial analysts, policymakers and researchers with system energy yield predictions as well as financial estimations of grid-tied renewable energy systems. The simulations are based on the system design parameters specified by the users[8]. This software is provided as a free download by NREL and is available with different programming languages[9]. It not only has a large data base for choosing modules and inverters, but it also provides the users with much freedom to specify the system parameters. One drawback of SAM is that it cannot perform simulations for some innovative PV devices such as tandem cells. It does not consider a design with reflectors either. The preset American laws and economic models also makes it less suitable in other regions.

The **Hybrid Optimisation Model for Electric Renewables (HOMER)** is also developed by NREL but later optimised and promoted by Homer energy. It is designed for micro grids using a combination of PV energy, wind energy and genset[10]. Except the availability to consider multiple sources and loads and to analyse the financial aspects, it is also known as being good at sizing and optimising. In HOMER, simulations run automatically time after time to decide on the optimal system configurations and component sizes. However, HOMER is only available for conventional silicon cells and does not consider a design with reflectors either.

These tools and other existing commercial yield prediction tools have precise estimation for monofacial silicon modules, but their prediction for bifacial modules still have certain error margins. Considering bifacial solar modules are gaining a greater mark share of the photovoltaic devices and need precise yield predictions, some research groups have developed yield prediction models available with bifacial designs of PV modules. At Energy research center of the Netherlands (ECN), a yield prediction tool called **BIGEYE** has been designed for bifacial PV systems[11]. **IEMC** has also developed a prediction model available for bifacial PV system[12]. These models do not include reflectors either like the aforementioned yield prediction models.

1.2. Introduction to Tandem Cells

Yield prediction models should not only be available for conventional solar cells, but they are also expected to be ready for the next generation of PV technologies, the tandem cells. Here this section introduces one of the most promising tandem concepts: perovskite / c-Si tandem.

1.2.1. Background

Currently single-junction solar cells are the most developed photovoltaic technology and dominate the solar cell market. This kind of cells have been studied for years and have achieved a great progress in increasing their light to electric power conversion efficiency (PCE), which keeps approaching the theoretical limit. This limit, is often known as detailed balance limit or Shockley-Queisser (SQ) limit, first put forward by William B. Shockley and Hans-Joachim Queisser in 1961[13]. Besides these traditional silicon-based photovoltaic technologies, recently new semiconductor materials and novel cell structures have attracted people's interest. One of the hottest topics in the material science is hybrid organic-inorganic perovskites.

Perovskites are a type of compounds with the same crystal structure as calcium titanium oxide and they can be described by the general chemical formula ABX_3, where A, B and X represent certain chemical elements. In the family of perovskites, organometal halide perovskites are a particular class of focus with A as $CH_3NH_3^+$, $HC(NH_2)_2^+$ and/or Cs^+, B as Pb and/or Sn and X as I and/or Br. They show a lot of advantages in terms of optical and electrical properties[14], such as a long diffusion length and a high charge-carrier mobility. Perovskite solar cells have impressed the solar industry by their rapid progress in their energy conversion efficiency. Their highest reported efficiency has increased from 3.8% in 2009[15] to 23.7 % in 2018[16], which is outperforming than that of CIGS-, CdTe- and Si-based solar cells. However, the record high-efficiency perovskite cells are Pb-based, which have some drawbacks as high toxicity[17]. Pb-free perovskite solar cells have therefore gained a great importance. Researches on Pb-free perovskites show that some alternative materials, such as Sn- and Ge-based halides, show attractive properties, but their PCEs are not as high as that of Pb-based perovskite cells. Of these alternative materials, Sn-based perovskites look most promising in the near feature to achieve similar PCE as Pb-based perovskites have[18], but its highest reported PCE is only 9.6 %[19]. Another drawback of perovskite tandem cell is that both Pb- and Sn-based perovskites show a poor stability. Due to their instability, the reported high-efficiency perovsktites are still in small sizes[20].

These drawbacks hold perovskite tandems back from commercialisation, but they are still an exciting field of study due to their high efficiency yet low costs. A growing number of researches are carried out to develop perovskite solar cells and the high-efficiency potential of these cells are of interest especially under realistic conditions. Perovskite solar cells are also regarded well suited to be the top cells in silicon-based tandem configurations, owing to their remarkable properties of adjustable band gap and larger band gap compared to silicon cells[21]. Perovskite/Si tandem cells have been reported to reach a 28 % PCE[22] and show a potential of even higher PCEs. They are an important application of perovskite solar cell and an interesting field of study, of which the working principle and current status are introduced in the following sub sections.

1.2.2. Working Principle

Tandem solar cells combines sub cells with different band gaps to make the best use of the incident light. An illumination of their working principle is given in Figure 1.3, where wide-bandgap material is represented by blue and narrow-bandgap material represented by red. The wide-bandgap layer absorbed higher-energy photons, while lower-energy photons travel through this layer and are absorbed by the narrow-bandgap layer. As perovskite solar cells have a wider band gap (for example it is 1.5 - 1.61 eV for $CH_3NH_3PbI_3$[23]) than silicon solar cells have (usually 1.12 eV), they can be optically stacked on silicon cells to act as the wide-bandgap sub cell.

Except the 2-terminal architecture shown above, there are also some other cell configurations applied for the perovskite/Si tandem solar cells. They are mainly reported in three forms: (1)2-terminal monolithic tandem, where cells are connected electronically in series and current matching is required; (2)2-terminal module tandem, where top and rear cells are mechanically stacked but electrically wired in parallel; (3)and four-terminal tandem, where sub cells are only electrically independent but optically stacked. A schematic illustration of these cell configurations is represented in Figure 1.4[21], with 2-terminal monolithic tandem, 2-terminal module tandem and 4-terminal tandem from left to right.

Of these three kinds of tandem configurations, 2-terminal monolithic tandem, which is named as series tandem in Figure 1.4, is the simplest yet most common design. The two sub cells in it are

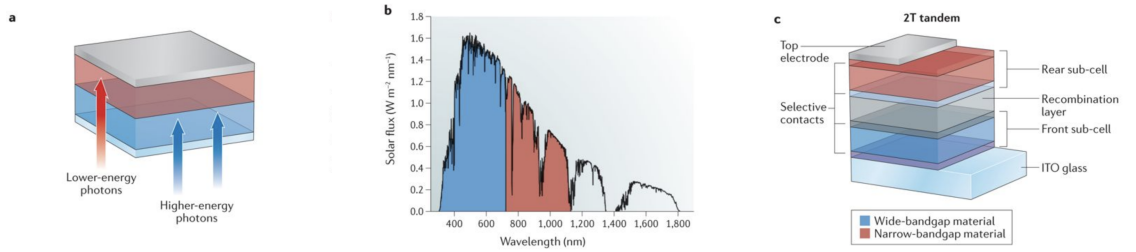

(a) Tandem solar cell concept.

(b) Solar irradiance spectrum showing useful parts absorbed by wide-bandgap and narrow-bandgap sub cells.

(c) Architecture of 2-terminal tandem cells.

Figure 1.3. Illumination of the working principle of the tandem cells[24].

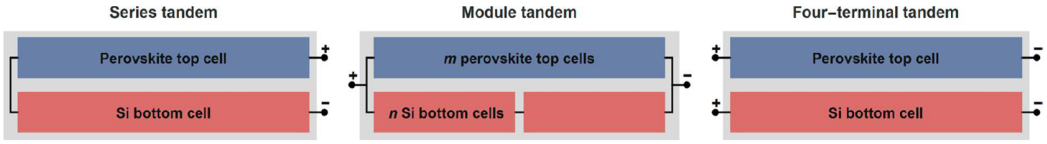

Figure 1.4. Perovskite/Si tandem cell configurations.[21]

optically dependent and electrically connected in series. The monolithic tandem cells sum up the voltages provided by top and bottom cells but take the lowest photo-generated currents between these sub cells as the cell current. Since this kind of tandem cells only needs one transparent electrode on the top side of them, their optical loss is lower than 4-terminal configurations and their costs are lower as well. The second kind of perovskite tandems is module tandem cells, in which the perovskite and silicon sub cells are also both optically and electrically dependent. As here the top and bottom sub cells are wired in parallel, the tandem sum up currents generated by top and bottom cells and get a larger cell current. As for the voltage, m perovskite top cells are series-connected while n silicon bottom cells are series-connected, in order to achieve voltage matching. The last kind of perovskite tandems given in Figure 1.4 is mechanically stacked four-terminal cells. These cells are free from the current mismatching or the voltage mismatching, therefore each sub cell can work at their maximum power point (MPP). They also enjoy more freedom in terms of determining different combinations of band gaps compared to other two kinds of cells. A drawback to them is that they need electrodes between the sub cells, which are required to be transparent to the incident light and have a good electrical conductivity at the same time. This may increase the cost and make them less competitive. Except these three configurations of perovskite tandems, there are some other cell configurations available for perovskite tandems. Here only these three common configurations are introduced. Of these three configurations, the 2-terminal monolithic tandems are considered as the least stable against spectral and temperature variation[21] due to the need of current matching. However, as this configuration is simple yet has a high efficiency, they have gained lots of interest and in this report, the perovskite/Si tandem cells specifically refer to the two-terminal monolithic cells.

Another unique feature making perovskite solar cells as ideal top cells in tandem configurations, is that their band gaps can be adapted. According to optical properties of the considered cell configurations, such as thicknesses and materials of layers, band gap of perovskite layer is tuned in order to achieve a highest cell efficiency. Therefore, they are preferred by the tandem configurations.

1.2.3. Current Status of Tandem Modules

Theoretically, the Shockley-Queisser limit for a tandem solar cell comprised of two sub cells is 45 %, compared to 34% for a silicon single-junction cell[25]. The highest efficiency of perovskite tandems have been reported to be 28 %[22] as mentioned above, but the efficiency under realistic conditions has not been measured yet. Futscher shows that under realistic conditions 2-terminal module tandems and 4-terminal tandems show a higher efficiency than conventional silicon cells, while 2-terminal monolithic tandem show a higher efficiency in some of the studied locations but a lower efficiency in other studied locations compared to silicon cells[25]. This is due to the fact that when taking realistic conditions into consideration, the performances of 2-terminal monolithic tandem cells are influenced by undesirable cell resistances, parasitic absorption, non-radiative recombination and current mismatching. In order to analyse the influence of these factors and therefore to optimise the cell structures, a prediction model to model the performance of perovskite/Si tandem cells under realistic meteorological conditions is needed, considering the influence of spectral variations and temperature changes in the real-world climate conditions.

1.3. PV System Prediction Model developed in TU Delft

Several tools, which analyse the performance of different parts of PV systems, have been developed inside the Photovoltaic Materials and Devices (PVMD) group at Delft University of Technology. Based on these tools, Garcia-Goma, a former student in the PVMD group, built a novel PV system yield prediction model in his MSc project "Development of Cell to System Annual Energy Yield Toolbox for Bifacial Modules"[26], which is referred as "Toolbox" in this report. After the first version developed by Garcia-Goma, Garro Etxebarria, also a MSc student in the PVMD group, developed the version 2 of the Toolbox by adding some new features and correcting some mistakes.

1.3.1. Toolbox Composition

The Toolbox comprises three models: the 'Cell Technology' Model, the 'System Setup Model' and the 'Location Integration' Model, which are in charge of different layers of the PV system. The layout of the Toolbox is given in Figure 1.5.

The 'Cell Technology' Model studies the cell structure and simulates light interaction inside the cell, based on the optical characteristics of a solar cell, including the layer thickness, roughness, refractive index and extinction coefficient. Of the optical models, a package called *'GenPro4'*, developed by Santbergen et al [27], is chosen for the Toolbox. GenPro4 calculates reflection, transmission and absorption of each layer of a solar cell, dependent of wavelengths and angle of incidence (AOI). This package is also available for bifacial solar cells as for bifacial cells the simulations are repeated with light incident on the back side, corresponding to the fact that bifacial cells can make use of both front and rear irradiation. This approach is regarded feasible as the front and rear light do not interfere with each other. After simulations on both sides, the absorption, reflection and transmission of this cell as a function of AOI and wavelength, are exported as the output of the Cell Technology model.

The following model, called 'System Setup' model, makes use of optical properties of a single cell given by the 'Cell Technology' model to characterise the performance at the module level. The cells are first arranged considering a given module configuration, in order to build a model of the stud-

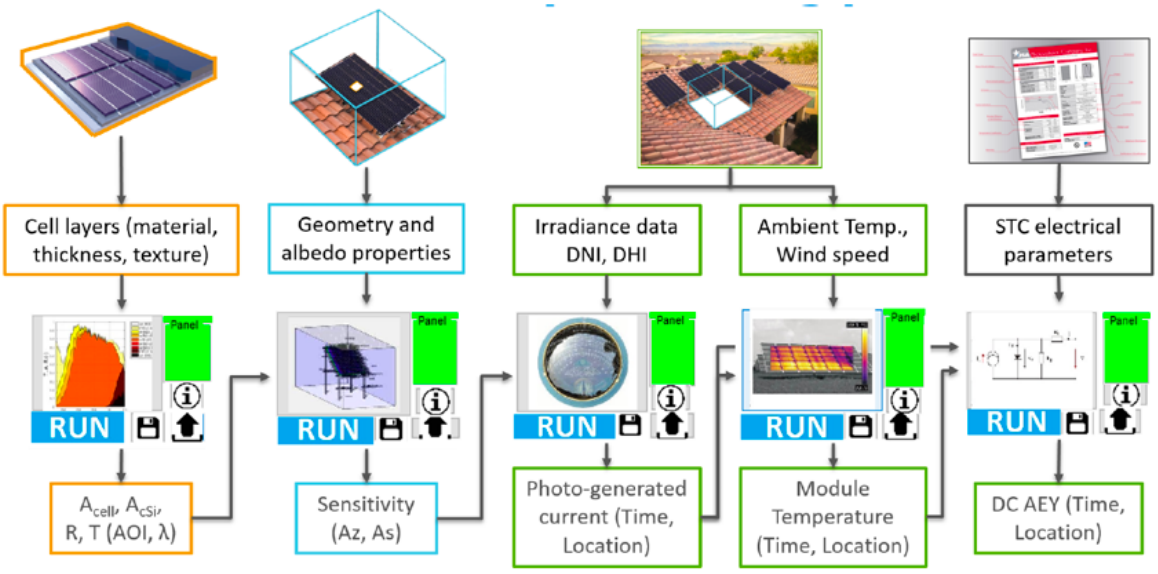

Figure 1.5. Toolbox layout with Cell Technology, System Setup and Location Integration model shown in orange, blue and green respectively.

ied module. This module are sealed with encapsulation material and be protected by two pieces of glass on the front and back sides of this encapsulated module. Later, if users would like to use reflectors, they can add reflectors in the model according to the position and tilt angle of the reflectors. At last, mounting frames are assembled under the four corners of the module. With this model, relative available light on each cell under different irradiance conditions is calculated. The results are then plotted in the form of a circle, named sensitivity map. Each point on the map indicates a certain solar position and value at that point illustrates the cell sensitivity to the incident light. The rays tracing, the calculations and plotting of sensitivity map are done by an in-house software *'Lux'* designed by Santbergen[28]. Compared to other available commercial softwares like LightTools, this software has an advantage that it can provide maps for infinite arrays of PV modules.

The last model is called 'Location Integration' model, which applies the module model to an actual operating environment. In this model, optical, thermal and electrical models are involved. Optical model, also called the Sky model, considers the utility of direct normal irradiance (DNI) and diffuse horizontal irradiance (DHI) obtained from weather data sources such Meternorm. In this model, the sky is divided into numerous sky elements according to the azimuth and altitude resolutions and the irradiance incident from each element are plotted in the Sky Map. Except for the ambient conditions, it is also necessary to consider shading impact caused by surrounding environment. Shading posed by the surrounding trees and buildings is considering according to the principle of the horicatcher, which considers skyline of the studied location and corrects the irradiance incident to the module[26]. The effect of mutual shading and reflection is simulated in the process of ray tracing. Integrating the product of sensitivity map and sky map gives the irradiance absorbed by the solar module. In addition to the irradiance level, the module performance is highly affected by the module temperature, so that it is also simulated by the Toolbox, to be more specific, in the Thermal Model. The causes of varying module temperature are considered in three ways, meteorological conditions, mounting structure and power flow in the circuit. As meteorologic conditions taken from weather data base like Meteonorm are hourly data, which is longer than the time constant of 7 minutes that a PV module needs to reach 63 % of the final temperature[29], Steady State models are used in thermal analysis. The normal module operating temperature (NMOT) model along with the

fluid-dynamics model are used in the Thermal Model and module temperature is given as a function of time and location. The last part of the 'Location Integration' model is the electrical model. In this model, I-V curves of the module are simulated based on the absorbed irradiance and electric properties of the module and DC output power is given as the output. By performing the simulation with annual weather data, the DC annual energy yield (AEY) could be predicted by the Toolbox.

1.3.2. Features and Limitations

While currently common prediction models are only suitable for monofacial modules, the Toolbox has extended the scope of application to both monofacial and bifacial cells. This is one of the advantages of the Toolbox compared to its competitive models, as bifacial solar cells have already been utilised in some practical projects and there is a need to make a precise prediction of their energy yield. Besides, the Toolbox is able to involve reflectors in the PV system design, which is an important feature of the Toolbox, as reflectors have been widely used in bifacial PV systems. The last feature of the Toolbox is that it considers mutual shading caused by the neighbouring modules.

However, there were some limitations of version 2 of the Toolbox. The first limitation was the Toolbox was only available for single-junction silicon solar cells and could not analyse the performance of tandem cells yet. Similar to bifacial cells, perovskite/c-Si tandems are a hot topic of the novel PV devices and have attracted a lot of attention. Although this kind of cells are still at the experiment phase, they have impressed the photovoltaic industry by their fast progress in the maximum energy conversion efficiency and are regarded with potential for even higher efficiency. To convince the market of this, energy yield predictions are necessary. In addition, there are many studies about optimising the tandem cells' performance and a prediction model can help valuate the results of the optimisation. Therefore, it would be useful if the Toolbox is available for tandem cells as well.

Another limitation of Toolbox was the problem that it neglected the influence of the solar spectra. The Toolbox averaged the wavelength-dependent absorption without considering the realistic distribution of spectral irradiance. In reality, spectral irradiance is different between wavelengths, therefore the cell absorption at different wavelengths is not equally important as well. When the sun is at different zenith angles, its spectrum varies accordingly, leading to a varying distribution of spectral irradiance and varying importance of cell absorption at different wavelengths. As the version 2 of the Toolbox attached equal importance to all wavelengths, the total cell absorption was not correctly predicted. Instead, the wavelength-dependent absorption need to be weighted according to spectral irradiance distribution. This could be even more important for the cases of tandem cells.

The last limitation of the Toolbox was that it did not consider the different performances between solar cells but took the average generation of the cells as the generation of the entire module. Cells can behave dissimilarly due to many influencing factors, such as mutual shading caused by the neighbouring modules and reflection from the ground or mounting frame. To measure the cells' performances, Toolbox calculated the sensitivity of each cell to the incident light, which was actually the ratio of absorbed rays to the total incident rays,

$$sensitivity = \frac{absorbed\ rays}{incident\ rays}. \tag{1.1}$$

These sensitivities were then averaged by the Toolbox and the average sensitivity was regarded as the module sensitivity. When the sun is in a high elevation and all cells are completely illuminated, this method is adoptable with only a small error. However, when some of the cells are partly shaded, or even worse when some are completely shaded, the module might be unable to function properly.

Especially when cells are connected in series, the current is determined by the cell with the lowest current, which actually corresponds to the lowest sensitivity. In order to predict the accurate photo-generated current through the module, the different performances between the cells need to be taken into account.

1.4. Objective of The Thesis

Based on the Toolbox developed in the PVMD group, this thesis aims to develop a version 3 of the Toolbox and verify its validity. Therefore, the main research goal is:

Improvements and experimental validation of a PV system performance prediction model–the PVMD Toolbox.

To realise this research goal, several sub goals need to be achieved as listed below:

Goal 1: Improve the Toolbox
The toolbox design has already been finished, but it can be improved by adding new features and increasing the accuracy. As for adding new features, the previous version could only be used for monofacial and bifacial single-junction silicon cells, so the version 3 will be modified to be available with other novel solar cells or even to allow the users to decide their own cell structures. To improve the accuracy, there are several things taken into account, including considering the influence of actual solar spectrum and analysing cell performances individually to consider the mutual shading.

Goal 2: Validate the Toolbox
As the Toolbox is still in the experimental stage, it is time to carry out experimental validation. The second goal of this thesis is to validate the toolbox via comparing the simulation results with measurement data taken from the PVMD monitoring system. Reasons of inaccuracy will be analysed as well.

Goal 3: Perform case studies with the Toolbox
The applicability to the perovskite/c-Si tandem cells is one of the important new features of this version of the Toolbox. Therefore, the third objective is to apply the improved Toolbox to predict energy yield of a tandem solar module and compare it with that of a conventional single-junction silicon module.

1.5. Outline of The Thesis

There are five chapters left in this report. Chapter 2 and 3 are both about the improvements of the Toolbox, with Chapter 2 focusing on the optical field and Chapter 3 dealing with problems in the aspects of thermal-dynamics and electronics. Chapter 4 aims to validate the accuracy of the Toolbox, by comparing the simulation results with the measured data. Chapter 5 will apply the Toolbox to perovskite/Si tandem cells by performing case studies. Finally, Chapter 6 summarises the works and gives recommendation for future studies.

2

Improvements of the Optical Model

This chapter describes the improvements performed on the Optical Model of Toolbox. Basically, it gives solutions to the limitations mentioned in Section 1.3.2. First, Section 2.1 deals with the problem of adding tandem devices as new objects. Later, Section 2.2 describes the modification to include solar spectra in the Section 2.3 describes the change to analyse the cells individually, followed by Section 2.4, where a brief conclusion is given.

2.1. Adaption To Tandem Solar Cells

This section deals with multi-junction solar cells. This is illustrated by using a popular example of multi-junction solar cells: the perovskite/c-Si tandem cell. This section first briefly introduces the cell structure of the perovskite/c-Si tandems included in the Toolbox and later describes the corresponding modifications in the Cell Model. Finally, an example of simulation results of the new Cell Model is given.

2.1.1. Tandem Solar Cell Structure

Perovskite/c-Si tandem devices have several cell configurations as introduced in Section 1.2.2. Of these configurations, the 2-terminal monolithic tandem has the simplest design yet a high-efficiency potential, so in this version of Toolbox it is taken as an example of the perovskite tandems while the other types of perovskite tandems are suggested for the future versions. Besides, perovskite tandems are also very flexible in terms of layer materials, thicknesses and textures. Figure 2.1 shows a general cell configuration of the double-glass 2-terminal monolithic perovskite tandems, with optical constants taken from literature[30].

In this figure, the layer materials and the ranges of their thicknesses are given. In the order of light travelling through, the 2-terminal monolithic tandem consists of several parts: the anti-reflective coating (ARC) of magnesium fluoride (MgF_2), the transparent conducting layer indium tin oxide (ITO), the hole transporting material (HTM) layer Spiro-OMeTAD, the perovskite layer, the electron transporting material (ETM) layer C_{60}, ITO, silicon hetero-junction (SHJ) bottom cell, ITO and the bottom electrode A_g.

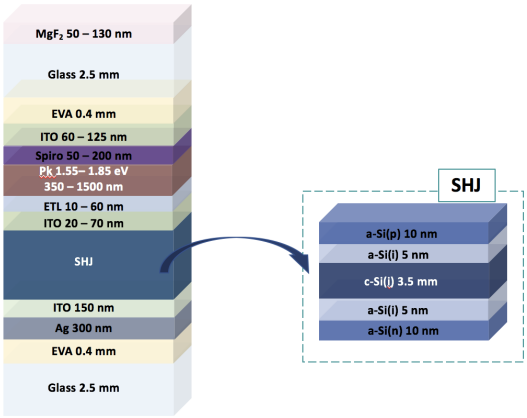

Figure 2.1. Cell configurations of the 2-terminal monolithic perovskite/c-Si tandem devices, and the SHJ bottom cell inside it, taken from [30].

2.1.2. Modifications in the Cell Model

To make Toolbox compatible with perovskite tandems, modifications were carried out on the Cell Model. As the input of the Cell Model is the cell configuration, including material, thickness and texture of each layer, the first modification is to build a default cell model of perovskite tandems with these optical input data. This default cell was mainly based on the structure given in Figure 2.1, except using a perovskite layer with a specific band gap energy of 1.65 eV. The thickness of the perovskite layer was then adjusted to achieve the current matching between perovskite top and SHJ bottom cell.

In this version of Toolbox, data bases were built in each model, to hold different sub models that Toolbox provides with the users. In the Cell Model, for example, a database was built to hold all types of cell structures available for simulations so that users can easily choose their desired cell structures. Despite this default structures, users could also define their cell structures following the examples given by Toolbox. They can customise the cell configurations by adjusting the layer thickness, adding texture and using other materials, like replacing C_{60} with TiO_2. The wavelength-dependent complex-valued refractive indices are already included in Toolbox, so users do not need to measure these values themselves. Figure 2.2 shows the User Interface (UI) of the Cell model. It can be seen that now Toolbox could simulate the module performance for monofacial SHJ cell, bifacial SHJ cell and perovskite/c-Si tandem cells.

2.1.3. Simulation Results

In the Cell Model, reflection, transmission and absorption in each layer are calculated at different wavelength interval and under different angles of incidence. These values are computed by GenPro4 developed by Dr. R. Santbergen, which as introduced in Section 1.3, is used to calculate absorption in each layer[27]. Example of simulation results of GenPro4 are given in Figure 2.3, which shows the wavelength-dependent absorptions of conventional SHJ cell and the reference tandem cell when the light is incident perpendicularly. The white area and the darkest area show the reflection and transmission respectively while the other coloured areas show the absorption in each layer.

As it can be seen from the figure, both of these two cells absorbed photons within a wavelength band from around 400 nm to around 1100 nm. While in the single-junction silicon cells, these pho-

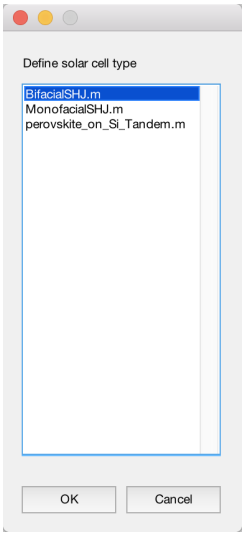

Figure 2.2. User interface (UI) of the Cell model.

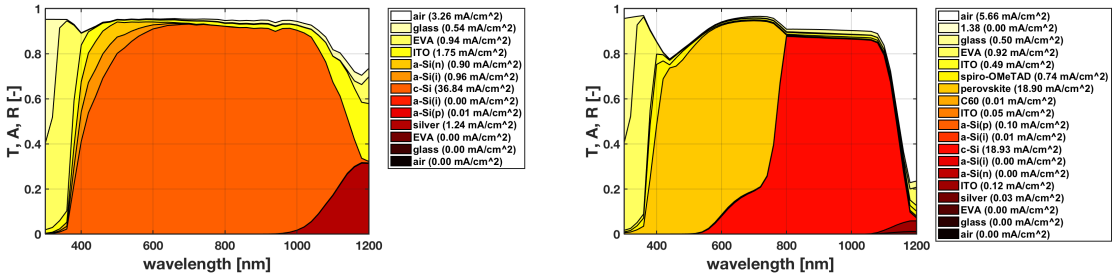

(a) Absorption of single-junction cSi cells

(b) Absorption of perovskite/c-Si tandem cells

Figure 2.3. Absorption of single-junction cSi cells and perovskite/c-Si tandem cells when light is incident perpendicularly.

tons were mainly absorbered by the c-Si layer, in the perovskite tandems, the two absorber layers, perovskite and crystalline silicon layer, absorbed different parts of light. As perovskite has a wider band gap, it can take full advantage of high-energy photons so that the spectral mismatch could be reduced and therefore the ultimate efficiency is increased. The SHJ bottom cell absorbed low-energy photons, as they can not be utilised by the perovskite layer.

As photons were divided between the perovskite and c-Si layer in the perovskite tandems, while in the single-junction silicon cell c-Si layer generated a photo current density of 36.84 mA/cm^2, the two absorber layers in the tandem cell, perovskite and c-Si layers could only generated nearly two-times lower photo current density of 18.90 mA/cm^2 and 18.93 mA/cm^2 respectively. Considering for the 2-terminal monolithic tandems, cell current is limited by the lowest sub cell current, the current density generated by the perovskite tandem was only 18.90 mA/cm^2. However, as the perovskite tandems have a more than two-times larger voltage than the single-junction cells, which compensates the lower photo current, normally they show a higher efficiency under STC than the conventional single-junction cells. To eliminate the influence of current mismatching between the sub cells, the thickness of the perovskite layer is tuned for current matching. For the studied tandem cell, this thickness has already been optimised so that perovskite and c-Si layer generated similar photo current densities. If the thickness of perovskite layer changes or a perovskite layer with another band gap is used, the absorption curves shown in the figure as well as photo current generated by the perovskite tandems will vary from this result, but these alternative cell structures can also be

tested by Toolbox.

Besides wavelength, the angle of incidence (AOI) also plays an role in the absorption analysis. By varying AOI from 0° to 90°, the absorption can be described as a function of AOI as well. The relation between absorption and AOI is described in Figure 2.4, including example of the single-junction c-Si cell and the perovskite tandem. As it can be seen from the results, when AOI increased, both single-junction and multi-junction cell showed a lower absorption, as more light was reflected. These results show that the Optical Model has been adapted for tandem cells.

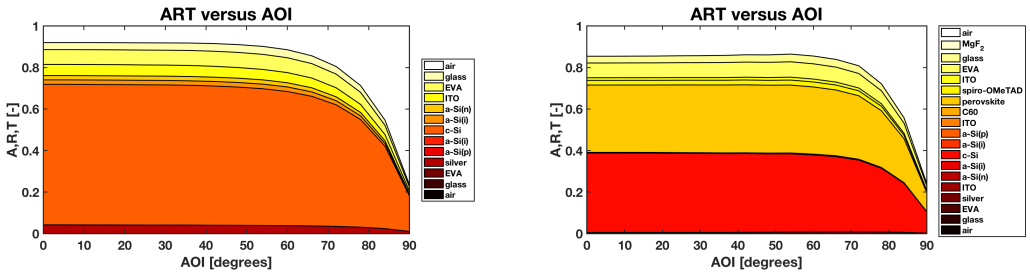

(a) Absorption of single-junction c-Si cells

(b) Absorption of perovskite/c-Si tandem cells

Figure 2.4. AOI-dependent absorption of single-junction c-Si cells and perovskite/c-Si tandem cells.

2.2. Consideration of The Influence of Solar Spectrum

This section corresponds to the second limitation of version 2 of Toolbox, which was caused by using a hypothetical solar spectrum instead of the real ones. The hypothetical solar spectrum assumed that all the wavelengths were equally important and took an equal share in the spectrum. This assumption simplified the calculations, however it also led to inaccurate predictions. To propose a possible solution, first real solar spectra will be simulated to compare different contributions of large and small wavelengths. Later, these spectra values will be employed in Toolbox to provide the users with a more accurate way to consider the influence of solar spectra. Lastly, an example case will be carried out to see the effect of the improvements.

2.2.1. Relevance of Solar Spectrum

The Earth's atmosphere acts as a filter filtrating the incident sunlight and has an impact on the solar spectrum. This filter varies continuously as its components such as moisture, gas composition and dust keep changing, leading to a varying solar spectrum. To simulate this varying solar spectrum, some modelling tools have been developed, one of which is the *Simple Model of the Atmospheric Radiative Transfer of Sunshine* (SMARTS) developed by NREL. It is a spectral model and Fortran code, which could predict irradiance and simulate spectral irradiance for surfaces with different geometries on the Earth's surface[31]. The solar spectra used in the following analysis and included in Toolbox both were simulated by SMARTS.

Solar spectrum is dependent on many influencing factors. Since air mass (AM) is the most important factor, for simplicity only AM is considered here. AM is the length ratio of the virtual path that the sunlight pass through the atmosphere to the possible shortest path, which is achieved when the sun is directly overhead. When the sunlight has to travel a longer distance to reach the Earth, there is a higher risk for it to be absorbed by the air and dust, which will result in lower irradiance levels

and a different spectral power intensity distribution. According to the definition, AM is determined by the zenith angle of the sun and can be calculated by the following function:

$$AM = 1/\cos\theta, \tag{2.1}$$

where θ is the solar zenith angle. Therefore, AM keeps changing according to the sun movement in a day. To compare the different spectra that different AMs result in, these AM-determined solar spectra were simulated in SMARTS and compared below. As Equation 2.1 is only valid when zenith angle is smaller or equal to 80 °, spectra simulations were only carried out for AM value accordingly from 1 to 5 in steps of 1 and also for AM1.5 as it is required by the STC. The spectral irradiance within wavelength range 300 - 1200 nm are represented in Figure 2.5. As defined in STC, all these simulated spectra corresponded to the sunlight incident on a sun-facing module tilted at 37 °.

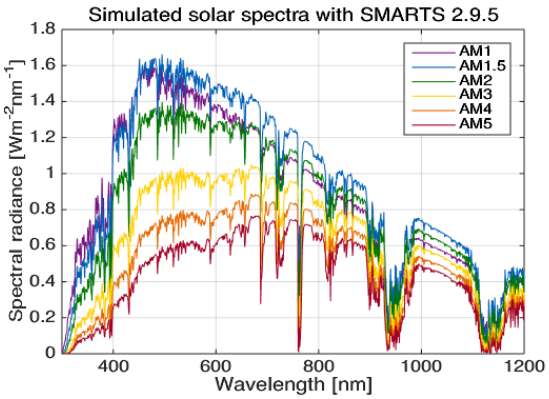

Figure 2.5. Solar spectra simulated by SMARTS 2.9.5[31].

Table 2.1. Spectral composition of the simulated spectra.

	$\%_{300-752\,nm}$	$\%_{775-1107\,nm}$
AM1	66.9	29.8
AM1.5	65.0	31.7
AM2	63.6	33.1
AM3	60.9	35.9
AM4	58.3	38.5
AM5	55.9	41.0
Hypothetical spectrum	55.2	35.6

The integration of spectral radiance is the total irradiance received by the Earth. As the figure shows, when AM is larger, the total irradiance is lower, corresponding to the fact that when the sunlight needs to travel a longer distance to take through the atmosphere, more sunlight is absorbed. Besides irradiance, the figure also shows that the spectral distributions of the irradiance varies with AM as well. Considering single-junction solar cells show relatively constant absorption within this wavelength range (see Figure 2.3), perovskite tandems are taken as an example to analyse the influence of spectral variation on cell performance. Therefore, the sunlight can be divided as blue light and red light corresponding to the band gaps of the perovskite and c-Si layer. To be more specific, as the studied perovskite layer has a band gap of 1.65 eV, the blue light refers to photons with wavelengths between 300 nm and 752 nm, which carries high-photon-energy light and is mainly used by the perovskite layer; on the other hand, considering the 1.12 eV band gap of c-Si layer, red light refers to photons with wavelengths between 752 nm and 1107 nm and absorbed by c-Si layer. The ratios of blue light and red light to the incident sunlight were also computed and results are tabulated in Table 2.1. The incident light has been normalised to have an integrated value as 100 % within a wavelength range 300 - 1200 nm. As it can be concluded from the results, when the air mass increases, or in other words when the sun gets closer the horizon, the ratio of the blue light decreases while that of red light increases. This implies a varying ratio of useful light for the absorber layers. Table 2.1 also compares the spectral distribution between the solar spectra simulated by SMARTS and the hypothetical spectrum used in versions 2 of Toolbox, which assumes that all wavelengths contribute the same to the solar spectrum so that spectral irradiance is the same at different wavelengths. It could be seen that with this hypothetical spectrum, the ratio of blue light was underestimated for most of time while that of red light always varied from the real spectra as well. This may result in inaccurate predictions of irradiance absorbed by the absorber layers.

2.2.2. Considering Spectral Distribution In Optical Models

In version 2 of the Toolbox, the AOI-dependent absorption was calculated according to the hypothetical spectrum. This spectrum attaches equal importance to all wavelengths and ignore the realistic spectral irradiance distribution. To accurately simulate absorption of the cells and therefore give precise predictions of photo-generated current, this version of Toolbox takes realistic solar spectra into consideration.

To achieve this, the first step is to regard the cell absorption not only dependent of AOI, but also dependent of wavelengths. This step is realised in the Cell Model. As described in Section 2.1, under a certain AOI, the previous version of Toolbox averaged absorption at different wavelengths and took these AOI-dependent absorption as the output of the Cell Model. However, in reality wavelengths contribute differently to the solar spectrum and their contributions also varies with solar zenith angle, as explained above. Using the hypothetical spectrum will result in incorrect predictions of photo-generated current. To solve this problem, instead of absorption only dependent of AOI, in this version of Toolbox the Cell Model gives absorption dependent of both wavelengths and AOI as an output.

These wavelength- and AOI-dependent absorption is used as the input for the following model, the Module Model. In this model, Toolbox simulates cells' sensitivities towards light incident from different angles of the sky dome considering a customised module layout. Due to the aforementioned modification carried out in the Cell Model, wavelength dependence of the absorption is now available for the Module Model as well. Instead of simulating a sensitivity map with the averaged absorption, Toolbox now simulates sensitivity map with wavelength-dependent absorption. This enables Toolbox to calculate wavelength-dependent absorption under real weather conditions in the next model, the Weather Model.

The most relevant modification to break this limitation is carried out on the Weather Model. In this model, Toolbox simulates the distributions of irradiance over the sky dome and generates a sky map. In version 2, the value of each element in the sky map was equal to the irradiance incident from that corresponding direction. However, version 2 did consider the spectral distribution. This problem was corrected in this version of Toolbox. Solar spectra data, within AM range 1 to 5.5, was simulated by SMARTS and included in the Weather Model. During simulations, Toolbox first calculates AM according to the solar zenith angle. According to AM, solar spectrum at the considered time is computed based on the solar spectra data. Based on the solar spectrum, spectral irradiance distribution of each sky element is simulated. The integration of the product of spectral irradiance and wavelength-dependent sensitivity is the irradiance absorbed by the cell. Finally, the absorbed irradiance is converted to the absorbed photon flux, which is the output of the Weather Model.

It is worth to notice that the spectra, included in the solar spectra data base inside Toolbox, were simulated for the case of a 37 °-tilted and sun-facing module, with which arrangement the AM1.5 spectrum is defined. For realistic conditions, photovoltaic modules are mounted at a adequate tilt and orientation according to the geographic conditions. This module arrangement is not necessarily the arrangement mentioned above, so the realistic spectral irradiance distribution might differ from those in the data base. From this perspective, Toolbox could mitigate the impact of varying solar spectra but it is hard to perfectly represent them in the simulation. As Toolbox serves as an DC energy yield prediction model for photovoltaic systems, if users want to determine the optimal module arrangement or to optimise cell structure via simulations, they can make certain assumptions and compare results with different system designs or cell design respectively. However, considering advanced users, who want to reproduce real life conditions in the simulations, it is recommended

to integrate SMARTS software with Toolbox in the future study.

2.2.3. Example Case

To compare the results of the old and new methods, an example is studied in this sub section. As the perovskite/c-Si tandem cell has two different absorber materials and is more sensitive to the changes in spectral irradiance, it was taken as the example in this case study. The tandem cell was put horizontally so that AOI was equal to solar zenith angle. By varying AOI, the AOI-dependent absorption was simulated, as shown in Figure 2.6. Figure 2.6(a) shows the result simulated by the old method, which averaged the wavelength-dependent absorption based on the hypothetical spectrum, while Figure 2.6(b) shows the result simulated by the new method, with which wavelength-dependent absorption was weighted averaged according to real solar spectra.

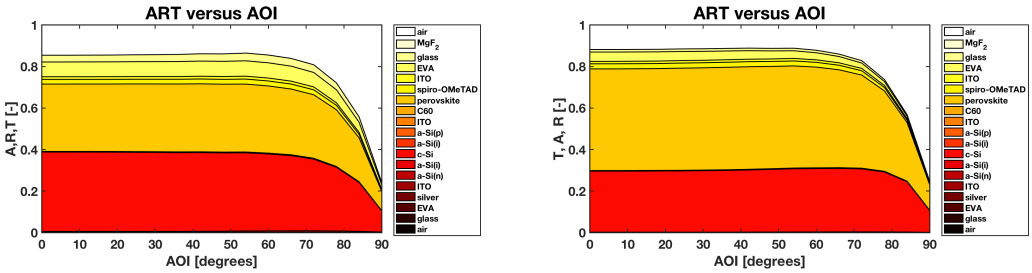

(a) Absorption versus AOI using the hypothetical spectrum

(b) Absorption versus AOI using real solar spectra

Figure 2.6. AOI-dependent absorption simulated based on the hypothetical spectrum and real solar spectra.

As it can be seen from the results, when the simulation took real solar spectrum into consideration, the AOI-dependent absorption was distinctly different from the one simulated by the old method, which took all wavelengths equally important. When absorption was averaged based on the real solar spectra, the dark yellow area, which referred to the absorption of the perovskite layer, was larger than that based on the hypothetical spectrum under most of AOI. The other absorber layer, c-Si layer, which was represented by the orange colour, showed slightly lower absorption when real solar spectra were considered.

To be more specific, the results at the AOI of 3 ° are compared. In the case of using the hypothetical spectra, the absorption of perovskite layer was 32.4 %. In the Cell Model, cells are assumed to be horizontal. Therefore, the 3 ° AOI indicated an AM1 solar spectrum. If the wavelength-dependent absorption was averaged weighted AM1 solar spectrum, the absorption of perovskite layer was 49.0 % instead. Therefore, the perovskite absorber could receive more energy than the hypothetical spectrum expected. Since in reality more photons were absorbed by the perovskite layer according to the real solar spectra, there were less photons absorbed by the c-Si layer consequently. According to the hypothetical spectrum, 38.2 % of incident photons were absorbed by the c-Si layer, while the AM1 spectrum implied that the c-Si layer only absorbed 29.4 % of the incident photons.

The deviation could be explained by the analyses above. According to Figure 2.3(b), the perovskite layer absorbs photons with wavelengths between 300 and 752 nm(referred as blue photons below) while c-Si mainly absorbs photons with wavelengths between 752 and 1107 nm (referred as red photons). The ratios of useful photons for these two absorber layers are given in Table 2.1. Comparing

the hypothetical and AM1 spectrum, it can be concluded that under AM1 spectrum blue photons occupy a larger ratio (66.9 %) than under the hypothetical spectrum (55.2 %); on the other hand, red photons occupy a smaller share under AM1 spectrum (29.8 %) than under the hypothetical spectrum (35.6 %). According to Table 2.1, the ratio of blue photons under the hypothetical spectrum is the lowest of the studied spectra, so using the hypothetical spectrum will overestimate the absorption of perovskite layer.

The difference between using the hypothetical spectrum and real solar spectra can also be seen from the module level. Take the module given in Figure 2.7 as an example. This module was 27 ° tilted and south-facing, with 60 cells connected in series. The sensitivity maps of the two absorber layers were computed and given in Figure 2.8.

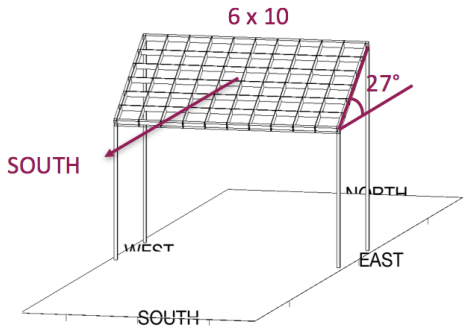

Figure 2.7. Example of module geometry.

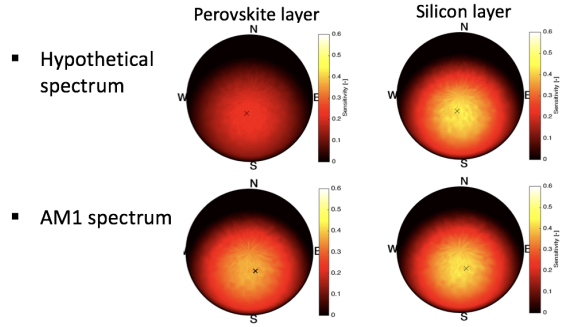

Figure 2.8. Sensitivity maps of perovskite layer and silicon layer considering different spectra.

This figure shows the sensitivity maps of perovskite layer and c-Si layer, with wavelength-dependent absorption averaged based on the hypothetical spectrum and AM1 spectrum. As explained in Section 1.3, a sensitivity map shows the cell absorption to the light incident from different elements of the sky dome. According to the simulation results, when the simulation was based on the hypothetical spectrum, the highest sensitivity of perovskite layer was 0.24 while that of silicon layer was 0.45, the positions of which were marked by the crosses. When the AM1 spectrum was used, the maximum sensitivity of perovskite layer was higher as 0.39 and that of silicon layer was almost the same as 0.44. This was consistent with the previous results, which indicates that under AM1 spectrum there are more blue photons available for the perovskite layer so that this layer show a higher sensitivity to the incident light, compared to the case where the hypothetical spectrum is used. On the other hand, as more photons are absorbed by the perovskite layer under AM1 spectrum, c-Si layer shows a lower sensitivity in comparison with the case using the hypothetical spectrum.

An example case is also studied for the Weather Model in order to verify the influence of using the hypothetical spectrum. A noon hour in a summer day was studied, with weather conditions taken from the Meteonorm data base[32]. According to the weather data, the global horizontal irradiance (GHI) was 376 W/m^2. With the sensitivity maps computed based on the AM1 spectrum, the total irradiance absorbed by the module was 348 W/m^2, of which 149 W/m^2 was utilised by the perovskite cell and 164 W/m^2 by the c-Si cell. In the case using the hypothetical spectrum, the module was predicted to absorb 344 W/m^2 irradiance, slightly lower compared to the former case. 92 W/m^2 of this irradiance was absorbed by the perovskite layer, which was much lower than the previous result and the error was high to 38 %. Silicon cell was predicted to absorb only slightly more irradiance as 166 W/m^2 with the hypothetical spectrum. In conclusion, realistic solar spectra should be considered in the simulations, especially when Toolbox is giving an prediction for the perovskite tandems.

It is worth mentioning that in reality, Toolbox considered the influence of real solar spectra in the Weather Model instead of in the Cell and Module Model, opposite to the simulations done above. In this case study, cell absorption is weighted according to the hypothetical spectrum and real solar spectra respectively, in both the Cell Model and Module Model. The result of the Weather Model, the absorbed irradiance mentioned above, is the product of this weighted/non-weighted average absorption and the incident irradiance. By doing this, this case study aims to give a deep research on how real solar spectra influence the cell performance from different perspectives. However, in the actual simulations of Toolbox, the Cell Model and Module Model keep the wavelength dependence and simulate absorption or sensitivity map for each wavelength. Real solar spectra are not considered until the simulations performed on the Weather Model, where the irradiance is distributed over wavelengths according to real solar spectra.

2.3. Individual Cell Analysis

This section describes the individual cell analysis added to the Toolbox.

2.3.1. Individual Cell Analysis

In the Module Model, cell sensitivity is calculated by performing ray tracing. In this process, mutual shading caused by the neighbouring modules could be simulated. This is a distinctive characteristics of Toolbox. However, this advantage has not been fully exploited. In versions 2 of Toolbox, the module performance was regarded as the average performance of the cells. This could be explained by the fact that the old versions of Toolbox assumed similar performances between the cells and neglected the influence of mutual shading.

The illumination differences between cells are easily to be omitted, as the cells have small surfaces (normally around 225 cm^2) and are put compactly. However, when there is shading or reflections from nearby modules, the irradiance incident on the cells can be non-uniform, resulting in different generations. Figure 2.9 showed an example of cells' sensitivities when the sun is close to the horizon. At this moment, the lowest row of cells are almost fully shaded. Module current is limited by the photo current generated in these shaded cells, thus the average absorbed irrdiance of cells could not indicate a realistic module current.

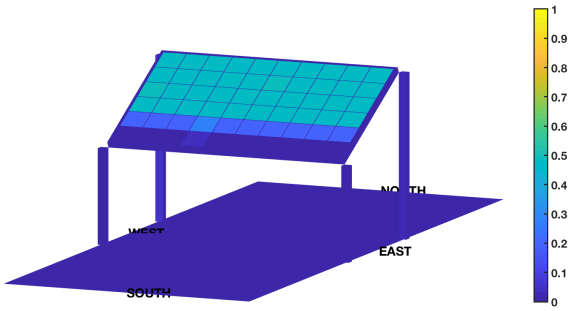

Figure 2.9. An example of cells' sensitivities when mutual shading exists.

The various illumination conditions have an influence on the energy yield prediction. Since the

photo-generated current is proportional to the irradiance level, varying illuminations would result in different photo-generated currents between the cells. For most commercial silicon solar modules, cells are connected in series so that the module current is determined by the lowest photo-generated current between the cells. However, commercial solar modules often have bypass diode it in order to avoid hot spots caused by the partial shading, which has not yet been considered in Toolbox. If bypass diodes are included in the future versions, the calculations of module current need to be modified according to the arrangement of bypass diodes.

2.3.2. Related Changes to the Toolbox

To analyse the cells individually, several modifications are required by the optical models and the electrical model. In terms of the optical part, as individual cell sensitivities have already been calculated in the Module Model, the correction to this Model is to take sensitivities of each cell into considerations and to simulate a sensitivity map for each cell. These sensitivity maps are used in the Weather Model to compute individual absorbed photons for each cell. The other related modifications to this limitation were performed on the Electric Model, which will be described in Section 3.2.

In order to analyse cell performance individually, it is important to give accurate prediction to each cell. The different absorption between cells can be caused by shading or reflection, but from the perspective of simulations, it could be influenced by some simulation settings as well. An influencing factor is the resolution of the simulation results. In the Module Model, for example, if a higher angular resolution is used in simulations, the sensitivity map is more accurate as it considers more precise sun positions. However, a proper resolution is a trade-off between accuracy and computational time. Users can decided the resolution according to their own requirements.

Another influencing factor exists in the rays tracing process and is analysed below. In the Module Model, the simulations of cell sensitivity are carried out by the package *Lux* developed by Dr. Rudi Santbergen inside the PVMD group. This package builds an unit cell according the module geometry defined by the users and simulates cells' sensitivities via performing ray tracing simulations. In these simulations, the number of rays per element (RPE) has an influence on the simulation results. The element refers to a group of cell expected to absorb identical irradiance. For example in a solar module, if each row of cells always absorb same irradiance, their individual sensitivity is close to the average sensitivity. Therefore, each row can be regarded as an element. If RPE is larger, it is believed that more rays hit an simulation element so that its sensitivity can be determined more accurately; while if RPE is too low, less rays are able to hit one simulation element, in which case it low absorption might be caused by inaccurate predictions instead of shading, reflection or influence of other weather conditions on the solar cells. RPE is a function of area of the simulation element and the density of rays emitted by the light source. This ray density is proportional to the number of rays emitted and inversely proportional to the area of the light source. Note that in this case the entire ceiling of the simulation domain (i.e. one unit cell) serves as the light source. Therefore the expected RPE is given by equation:

$$RPE = \frac{N_r}{S_{LS}} \times S_e. \tag{2.2}$$

RPE shows the number of available rays assigned to one simulation element in ray tracing. As Toolbox considers cells' performances individually, the simulation element is each cell here. To analyse the influence of RPE, sensitivity calculations were perform on a 60-cell module with a series of RPEs. As the studied module was put horizontally and rays were perpendicularly incident, cells in

this module were expected to have a uniform sensitivity. However, the simulation results show that cells had different sensitivities and this difference varied with RPE as well. To quantify the influence of RPE, the standard deviations (SD) of cell sensitivities under different RPE were calculated. An SD of 0 implies that the cells share a uniform sensitivity, which is expected theoretically. As rays are distributed evenly but randomly over the entire ceiling, these simulations were repeated for 100 times to avoid extremely-deviated results. A box plot of the results is given in Figure 2.10 with standard deviation expressed logarithmically.

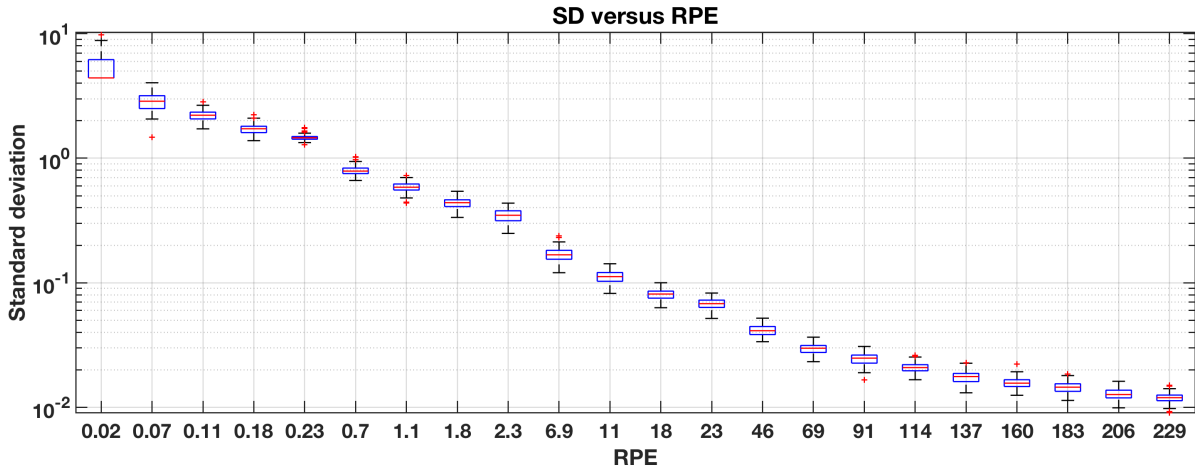

Figure 2.10. The standard deviation of cell sensitivities simulated under different RPE. The standard deviation is expressed in the form of logarithm.

The influence of RPE is analysed from two perspectives: uniformity of cells' sensitivities and reproducibility of the simulations. In terms of uniformity, under each RPE, the medium value of SDs given by the 100 repeated simulations was taken as the representative SD at that RPE (expressed by the red line in each box). As explained above, theoretically these SD should be equal to 0 so that SDs which are closer to 0 show that the corresponding RPE gives a more accurate prediction. By comparing the representative SDs under different RPEs, it could be demonstrated that with an increasing RPE, SD of cell sensitivities decreases, indicating a higher accuracy. Increasing RPE could greatly improve the accuracy when the RPE is relatively low, but when the RPE is already high, the gain in accuracy is much smaller.

In terms of reproducibility of the simulations, under each RPE, not the medium value but the deviation of the SDs given by the repeated simulations was analysed. With a same RPE, repeating the simulations should give a same SD of cells' sensitivities. If results of SD given by the repeated simulations vary a lot, it can be concluded that the reproducibility of the simulation is low. Therefore, the result given by the simulations is not reliable, as repeating the simulation will give another result. The deviations of simulation results can be seen by the length of each box. A large length of the box shows that there is a higher possibility that the repeated simulations give different results, leading to a lower reproducibility of the simulation. It can be seen from the figure that with an increasing RPE, reproducibility of the simulation also increases, indicating a more reliable simulation result. Therefore, it can be concluded that in order to achieve a more accurate and reliable simulation result, a higher RPE is required.

A high RPE can be achieved in two ways according to Equation 2.2. The first way is to increase the density of rays $\frac{Nr}{S_{LS}}$. For a module geometry with a predefined area of light source, this is done by increasing the number of rays used for ray tracing. However, this requires a longer computational

time. Another way is to increase the area of considered element S_e. In the case of analysing cells individually, element refers to one single cell, which, for a predefined geometry, is not possible to increase its area. However, if neighbouring cells are assumed to share a same sensitivity, they can be grouped together and taken as a simulation element instead. By grouping cells together, the area of simulation element multiplies, leading to a multiplied RPE. For example, if the neighbouring two cells are assumed to have same sensitivity, they can be grouped together. The simulation element therefore has a double area and double RPE. In the case of version 2 of Toolbox, as it assumed that all cells had same sensitivities, it took all the cells as one simulation element and used the average sensitivity instead. In order to analyse whether different groupings have influence on the relation between SD and RPE or not, an example analysis is given. The sensitivity of each element is the average sensitivity of cells inside it, thus SDs are computed as standard deviation of elements' sensitivities instead of that of the cells. The median value of SDs at each RPE was taken as the representative RPE-dependent SD. The SD-RPE relationships with different sizes of elements are given in Figure 2.11.

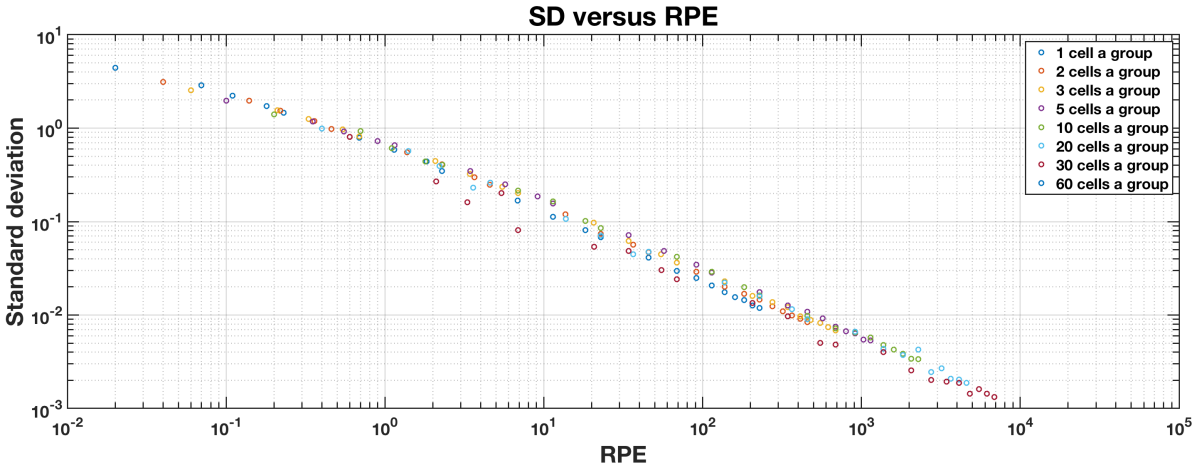

Figure 2.11. The RPE-dependent SDs of elements' sensitivities under different assumptions, with x- and y-axis both in the logarithm form.

The figure demonstrates that when the simulation element contains different amount of cells, it shows similar SD-RPE relationships between these cases, except the case when all 60 cells are group the SD is equal to 0. Therefore, under a same density of incident rays, grouping cells together and increasing the area of simulation element could have a high RPE as well, but by doing this the individual cell analysis is based on an assumption that some cells share a same sensitivity.

In conclusion, in order to give precise predictions of cell performances, there are some simulation settings need to be paid attention to, and RPE is one of these settings. A higher RPE ensures a better accuracy and reproducibility. Users can achieve a higher RPE by increasing the density of rays, but this will take a longer computational time;or if they assume some cells have same sensitivities, they can increase the area of simulation element. In this version, Toolbox provides users with two options, either to simulate individual sensitivity or to take all cells as a simulation element and simulate the average sensitivity. By using the average sensitivity, users assume that there is no or just a little influence of shading and reflection so that they can take all cells as one element and absorption is each cell is equal to their average absorption. This way could not only use less rays and therefore reduce simulation time, but could also ensure a high accuracy at the same time.

2.4. Conclusions

The goal of this chapter is to discuss the the limitations of version 2 described in section 1.3.2 and to provide solutions to them. The changes mentioned in this chapter are mainly performed on the optical models inside the Toolbox. The modifications related to these three limitations but performed on the Thermal and Electrical Models will be explained in the next chapter. Each subsection in this chapter corresponds to one limitation, arranged in the order they are mentioned before.

Section 2.1 dealt with the need of expanding the scope of application. The option to analyse the performance of perovskite/c-Si tandem devices was added to this version of Toolbox. The reference cell configuration was first described, followed by the description of modifications in the Cell Model. The optical properties of the reference cell were then simulated by the new version and analysed as well.

Section 2.2 was about the changes to mitigate the influence of realistic solar spectra. Solar spectra with a series of AMs were simulated by SMARTS 2.9.5[31]. These spectra were added to the Toolbox in order to consider the influence of realistic spectra during the simulations. After the improvement, the simulation results of the old and new version were compared in the example case study.

Lastly, Section 2.3 solved the need to analyse cell performance individually. Cells were proven to receive different amount of irradiance, which would result in differential current generation. Thus, it would be better to analyse the cell performance individually. Some simulation settings have influence on the accruary and reproducibility of the simulations, such as RPE. Users can increase RPE by increasing the density of rays or using average sensitivity of cells in this version of Toolbox.

3

Improvements of the Thermal and Electric Model

This chapter explains improvements carried out on the Thermal and Electric Models of the Toolbox and describes new methods involved in these models. In this chapter, corrections to the Thermal Model is first described in Section 3.1. Section 3.2 details the modifications in the Electric Model, including a new model to compute temperature coefficients and some corrections to this model. Finally, a brief conclusion is drawn in Section 3.3.

3.1. Improvements of the Thermal Model

This section contains the modifications carried out on the Thermal Model, which is a part of the Weather Model. The main purpose of the modifications is to make this model compatible with the aforementioned new feature of Toolbox, which is to analyse cell performance individually. Besides this, corrections to it are also described.

3.1.1. Glass Absorption

The Thermal Model inside the Toolbox integrates a thermal model developed by Faturrochman[33]. This model was built according to the thermal model put forward by Notton[34], which is based on the fluid-dynamic model but designed for double-glass photovoltaic modules. Since nowadays many solar modules are all protected by double glass against water, dust and dirt, this thermal model is suitable for the Toolbox.

In this thermal model, the absorption of both front and back glass is calculated in order to compute their temperatures. In version 2 of Toolbox, it was assumed that both front and back glass absorb 5 % of the total absorption. However, this 5 % ratio is an empirical value. To validate the accuracy of this value, first the absorption of front glass is studied. The ratio of front glass absorption to total absorption was simulated and plotted against AOI in Figure 3.1.

According to the results, for the three default cells, monofacial silicon, bifacial silicon and perovskite tandem cells, this ratio is around 1.4 percent and slightly deviates from this value under different AOI. Based on this result, in the Toolbox, the front glass absorption is adjusted to be 1.4 % of the total absorption.

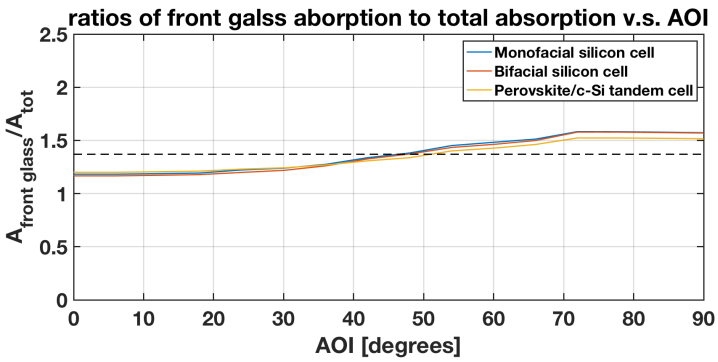

Figure 3.1. AOI-dependent front glass absorption compared to total absorption for three kinds of reference cell configuration.

The ratio of back glass absorption to the total absorption is different between these three kinds of cells. For monofacial silicon cells and perovskite tandem cells, as they have silver on their back side as their bottom electrodes, they are non-transparent to the incident light so that no light could be absorbed by the back glass. For bifacial silicon cells, the situation is different. Bifacial cells absorb irradiance incident from the back side, thus their back glass could absorb part of the light incident on the back side. According to simulation results, the back glass could absorb around 1.4 % of light incident on the back side. Although the back side absorption could be enhanced by being installed on a surface with a high albedo, such as the surface of the water, or installed with reflectors, its contribution to the total absorption is normally not very high. Therefore, for simplicity, the ratio of back glass absorption to the total absorption defaults to zero for all three kinds of reference cell configurations.

It is possible for Toolbox to simulate absorption of glass, but there are two reasons that Toolbox uses constant ratios instead. One of reasons is that, as it can be seen from Figure 3.1, absorption of glass varies little compared to the total absorption under different AOI. Another reason is that calculating exact absorption of glass will increase computing burden. Therefore, Toolbox assumes that the front glass always absorb 1.4 % of the total absorption and the back glass does not absorb light.

3.1.2. Cell temperature and module temperature

As shown in Section 2.2.3, cells could absorb different amount of irradiance due to shading or reflection. This could also introduce different temperature between cells as well. Considering this, the version 3 of the Toolbox allows the users to calculate the temperature of each cell individually. As the cross section area between the neighbouring cells is smaller compared to the contact area between the cell and the glass, the thermal conduction between neighbouring cells is neglected.

In addition to these modifications, some small mistakes were also discovered and corrected, for instance the equations to calculate radiative exchanges. As outputs of the Optical Models have been modified, the Thermal Model was also adjust to be compatible with these new inputs.

3.2. Improvements of the Electric Model

This section analyses modifications performed on the Electric Model. It first describes an additional tool to simulate temperature coefficients of open-circuit voltage and short-circuit current. Later,

corrections to this model are also explained.

3.2.1. Additional Model to Simulate Temperature Coefficients

A higher cell temperature can increase short-circuit current I_{SC} but decrease open-circuit voltage V_{OC}. This would affect the shape of I-V curves and result in a different output power. To consider this impact, it is important to take temperature coefficients of short-circuit current and open-circuit voltage into consideration. For commercial PV modules, these coefficients are often provided with the data sheets. Therefore, users can provide these empirical parameters directly.

However, as the application range of the Toolbox has been extended to tandem devices, which have not yet been commercialised, the temperature coefficients could not be taken from data sheets. Therefore, there is a need for Toolbox to include the simulation of temperature coefficients. To describe the relationship between temperature and the electric parameters I_{SC} and V_{OC}, a single-junction c-Si solar cell is taken as an example.

The short circuit current I_{SC}, is always approximated as the photo-generated current I_{ph}. For a solar cell, the current density J_{ph} can be described as a function of wavelengths λ and computed by

$$J_{ph}(\lambda) = \eta_\lambda e N_\lambda [35], \tag{3.1}$$

where η_λ stands for the quantum efficiency, e for the elementary charge and N_λ for the incident photon flux density. η_λ and N_λ are both wavelength-dependent. N_λ can be expressed as

$$N_\lambda = P_\lambda \cdot \frac{\lambda}{hc}, \tag{3.2}$$

and P_λ is the wavelength-responded power density. Therefore, the photo-generated current density J_{ph} is the integration of J_{ph} over the solar spectrum as

$$J_{ph} = \frac{e}{hc} \int_0^{\lambda_l} \eta_\lambda P_\lambda \lambda d\lambda. \tag{3.3}$$

In this equation, the limiting wavelength λ_l is determined by the band gap E_g as

$$\lambda_l = \frac{hc}{E_g}. \tag{3.4}$$

The band gap energy E_g is a temperature-dependent parameter. For the example of c-Si cells, a linear approximation can be made as

$$E_g(T) = E_g(300K) + \frac{dE_g}{dT}(T - 300K), \tag{3.5}$$

where $\frac{dE_g}{dT} = -2.3 \times 10^{-4} eV/K$ for c-Si cells[36]. With Equation 3.3, 3.4 and 3.5, the photo-generated current density can be computed. When the temperature goes up, there is a decrease in the band gap energy E_g. As a result, the limiting wavelength λ_l increases, leading to an increase in absorbed photons and therefore an increased photo current density J_{ph}. While varying the temperature from $-40\,^\circ$C to $90\,^\circ$C, which is the operating temperature range for many solar modules, the temperature coefficient of the short circuit current I_{SC} can be calculated.

Another temperature-dependent parameter of photovoltaic devices is the open-circuit voltage V_{OC}. Its temperature dependence is also a result of the variation of band gap energy. When temperature

increases, for absorber materials which band gap energy is decreasing, more electrons are able to overcome the band gap by thermalisation. These thermally-generated carriers increase the saturation current I_0. The temperature response of the saturation current can be described as[37]

$$I_0 = \propto exp(-\frac{E_g}{kT}). \tag{3.6}$$

For a typical silicon cell with an energy gap $E_g = 1.12eV$ under $T = 300K$, according to Eq.3.6 the temperature coefficient of I_0 is

$$\frac{1}{I_0}\frac{dI_0}{dT} = \frac{E_g}{kT^2}|_{T=T_0} = 14.5[\%/K]. \tag{3.7}$$

The saturation current I_0 has impact on the output current. Based on the equivalent circuit, the output current I_L under an external voltage V_a is

$$I_L(V_a) = I_d - I_{ph} = I_0[exp(\frac{qV_a}{nkT}) - 1] - I_{ph}. \tag{3.8}$$

When the cell is open-circuited, we have $V_a = V_{OC}$ and $I_L(V_{OC}) = 0$, thus it follows that

$$V_{OC} = \frac{nkT}{e} ln(\frac{I_{ph}}{I_0} - 1). \tag{3.9}$$

Considering the temperature response of I_0, Radziemska put forward that V_{OC} changes with temperature in the relation as[37],

$$V_{OC}(T) = V_{OC}(T_0) - [\frac{E_{g0}}{e} - V_{OC}(T_0)] - \frac{3kT}{e} ln\frac{T}{T_0}. \tag{3.10}$$

As $ln\frac{T}{T_0}$ varies little with different temperatures, the equation above can be approximated by a linear one

$$V_{OC}(T) \cong V_{OC}(300K) - const(T - 300K), \tag{3.11}$$

so the temperature coefficient of V_{OC} can be derived from Eq.3.10 as

$$\frac{dV_{OC}}{dT} = -\frac{(E_{g0}/e) - V_{OC}(T_0)}{T_0} - \frac{3k}{e}. \tag{3.12}$$

Therefore, the temperature coefficient of the open-circuit voltage V_{OC} can be calculated as well. So far the two necessary temperature coefficients can be obtained by simulations.

It is worth mentioning that, as the temperature dependence on I_{SC} is calculated based on the variation of band gap energy, it is crucial to determine the relationship between energy gap and temperature. For silicon solar cells, this value is around as mentioned above. For perovskite material, the situation is more complicated.

Some researches show that the relationship between perovskite's band gap energy and temperature is not linear[23]. An example is given in Figure 3.2, which shows temperature dependency of band gap energy for the methylammonium lead iodide ($CH_3NH_3PbI_3$) stablised wity poly(methyl methacrylate) (PMMA).

As the reference tandem cell also uses $CH_3NH_3PbI_3$ as the perovskite layer, this material is analysed below. $CH_3NH_3PbI_3$ experiences phase transitions when the temperature varies. When temperature goes down, $CH_3NH_3PbI_3$ shifts from the cubic to tetragonal phases at 327 K and further

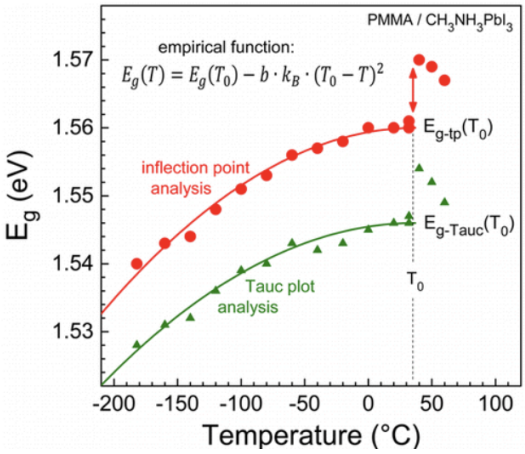

Figure 3.2. Temperature dependence of the bandgap of PMMA/$CH_3NH_3PbI_3$ [23].

shifts to the orthorhombic phase at 162 K[38]. As under realistic conditions, photovoltaic devices mainly work within a temperature range from −40 °C to 90 °C (around 235 K to 365 K), it could concluded that $CH_3NH_3PbI_3$ mainly exits in the tetragonal phase and sometimes in the cubic phase. For band gap energy E_g of the tetragonal phase of $CH_3NH_3PbI_3$, its temperature dependency can be described by an empirical quadratic function as

$$E_g(T) = E_g(T_0) - b \cdot k_B \cdot (T_o - T)^2, \tag{3.13}$$

where T_0 is the temperature that $CH_3NH_3PbI_3$ undergo a phase transition from the cubic to tetragonal phases and b is a unitless number[23]. For the band gap energy of the cubic phase of $CH_3NH_3PbI_3$, its temperature dependency is when the temperature is between 40 to 60 °C. For simplicity, temperature dependence of $CH_3NH_3PbI_3$ is approximated to be linear. As the tetragonal phase of $CH_3NH_3PbI_3$ was reported to have a band gap of 1.61 eV at 295 K and 1.54 eV at 160 K[39], the temperature coefficient of band gap energy is approximated as $\frac{dE_g}{dT} = -5.2 \times 10^{-4} eV/K$.

For now, Toolbox assumes constant temperature coefficients for all absorber materials. In the future work, it is recommended to accurately simulate temperature coefficients in different temperature ranges for the perovskite materials.

3.2.2. Corrections to the Electric Model

As mentioned in Section 1.3.2, in the previous version of Toolbox, the differences between cell performances were neglected and the average absorbed irradiance was taken to calculate the photogenerated current of the module. However, in reality, cells could absorb different amounts of irradiance due to shading and reflection and could have different temperatures, leading to different powers that cells can deliver. Therefore, the first correction to the Electric Model to analyse cell performances individually.

To achieve this, first all the electrical parameters are adapted to the cell level. Based on the data sheet, the short-circuit current I_{SC} and the maximum power point current I_{MPP} need to be divided by the number of parallel connections of cells N_p while the open-circuit voltage V_{OC} and the maximum power point voltage V_{MPP} are divided by the number of cells connected in series N_S. Accordingly, the series resistance R_S, the shunt resistance R_{Sh} and the saturation current I_0 could be simulated for one single cell, and the I-V characteristics of each cell are now possible to be simulated based on the Kirchhoff's laws. Accordingly the I-V characteristics of the module are simulated and

the resulting maximum power P_{mpp} is taken as the output power. Toolbox now only considers the situation that all cells in a module are connected in series. For some novel photovoltaic technology, such as the half-sized cell, solar module could have cells connected in parallel. It is recommended to consider parallel connections of the cells in the future versions of Toolbox.

As analysed in Section 2.3, cells could absorb different amounts of irradiance. This different absorbed irradiance directly influences the I-V characteristics of the solar cells. Figure 3.3 gives an example of different I-V curves between cells. The simulation was perform for a morning hour in May based on the real weather data. The factor RPE mentioned in Section 2.3 was set with a high value to exclude its influence on the simulation results. From this figure, it could be analysed that at the studied moment there is no distinct shading existing. The higher photo current in some cells might be caused by reflection from the ground or neighbouring modules. The average I_{ph} was 12.3 A while the lowest current, which in fact limited the module current, was only I_{ph} was 11.5 A. Therefore, when non-uniform illuminations exists, using the average absorption overestimates the module output.

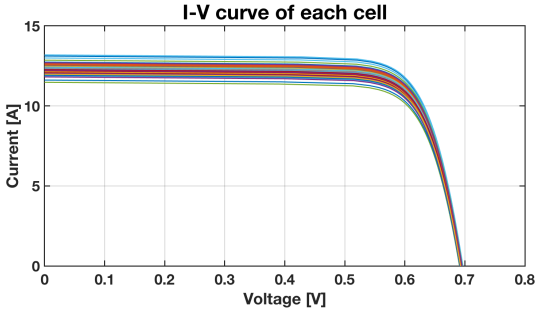

Figure 3.3. I-V curves of each cell at a moment in a summer day in May.

Except for being able to study different performances among the cells, another reason to simulate the I-V characteristics at cell level is that the sub cells in the tandem solar devices have different electrical parameters, thus the I-V curves of each sub cell are needed in order to compute that of the tandem cell. As many tandem devices are still in the test phase, the aforementioned electrical parameters, including V_{OC}, I_{SC}, V_{MPP} and I_{MPP} are asked for a single tandem cell instead of the whole module. As for now only monolithic tandem cells are considered, modifications are needed if other tandem configurations, like module tandem and four-terminal tandems are considered in the future.

The second correction to the Electric Model is about the calculation of the photo-generated current I_{ph}. In the previous version of Toolbox, it was calculated based on the linear relationship between the incident irradiance and I_{ph}, which indicated that a crystalline silicon cell can deliver a current density of 46.47 mA/cm^2 under STC. However, the 1000 W/m^2 irradiance under STC, is the incident power density for the solar modules while Toolbox computes the irradiance absorbed by the cells. Comparing this absorbed irradiance with the incident irradiance under STC will underestimate I_{ph}. On the other hand, the 1000 W/m^2-46.47 mA/cm^2 relationship is only valid for c-Si cell. For other absorber materials, for example the perovskites, an incident irradiance of 1000 W/m^2 may not generate a current density of 46.47 mA/cm^2, since they have different band gap energy and could absorb photons within different wavelength ranges. This shows the fact that this old method omits the influence of solar spectra. In this version of Toolbox, as explain in Section 2.2, the realistic solar spectra have been considered in the Weather Model and the absorbed photon fluxes are given as an input of the Electric Model. I_{ph} is therefore computed based on the absorbed photon flux.

Except the aforementioned two corrections, some other small mistakes were found and corrected. For example, in the sub model calculating series and shunt resistance, the index to determine the optimal solution was corrected. In addition, cleaning up of useless codes was also carried out and the outputs of each model were adjusted to the form of structure, making it clearer and better structured for the users and future studies of this project.

3.3. Conclusions

This chapter describes modifications to the Thermal and Electric Models. The modifications includes relevant changes to the topics discussed in Chapter 2 as well as some additions and corrections.

Section 3.1 was about the changes in the Thermal Model. The ratio of front glass absorption to the absorption was corrected from 5 percent to 1.4 percent and that of back glass absorption was set as 0. In addition, users can choose whether to calculate the average cell temperature as the module temperature or to calculate the temperature of each cell.

Section 3.2 discussed the changes in the Electric Model. First a new tool added to the Toolbox is described, which was used to calculate temperature dependence of V_{OC} and I_{SC} based on the way that band gap responses to the temperature. Later corrections to this model were listed, including simulating I-V characteristics for one cell and computing the photo-generated current I_{ph} based on the absorbed photon fluxes.

4

Validation of the Toolbox

This chapter aims to validate the accuracy of the Toolbox. Although the Toolbox has already been developed, so far it has not been validated with measurement data or simulation results from other prediction models yet. The validation was divided into two parts: (1)under Standard Test Conditions, (2)under realistic conditions. The former was done by performing indoor measurements while the latter was based on the measurements of a PV module mounted in the PVMD monitoring station. In this chapter, Section 4.1 first gives a brief introduction to the experiment setup. Later, Section 4.2 analyses the accuracy of the Toolbox by comparing the simulation results with the measurements. After the analysis, a conclusion is drawn in Section 4.3.

4.1. Experiment Setup

This section contains the background information of the system setups. It first describes the experiment setup of the indoor measurements, where the electrical characteristics of the solar module under STC were determined. Later it gives a brief introduction to the PVMD monitoring system, where the outdoor measurements were taken. The measuring methods used in this monitoring system are explained as well.

4.1.1. System setup of indoor measurements

The measurements of current-voltage curve are commonly used to evaluate the photovoltaic module performance. From the measurements, electrical performance parameters of the modules, such as open-circuit voltage V_{OC}, short-circuit current I_{SC}, voltage at the maximum power point V_{mpp}, current at the maximum power point I_{mpp} and maximum power output of the module P_{mpp}, can be determined. As these electrical properties are always provided by the manufacturers under STC, the solar module used for the validation was also first tested in the lab under STC to compare the real electrical properties with the values given by the data sheet. These measurements were performed on the solar module using the Large Area Solar Simulator (LASS) from Eternal Sun, which provides illumination of AM 1.5 and 1000 Wm^2 irradiance. Figure 4.1 shows this test equipment inside the PV Lab.

4.1.2. System setup of outdoor measurements

Except the indoor measurements under STC, the module performances were also measured outdoors under realistic conditions. The outdoor measurements were performed in the PVMD moni-

Figure 4.1. The Large Area Solar Simulator (LASS) used in the PV Lab to perform I-V curve measurements.

toring station, which is mainly used for the PV module measurements and relative studies inside the PVMD group. The monitoring station is located at the top of the co-generation plant inside the TU Delft campus and consists of several physical parts: the Egis tracker, a fixed rack, a Solys 2 tracker by Kipp & Zonen, weather station, two Maximum Power Point Tracking (MPPT) enclosures, the PV Measurement Unit (PVMU) built by Laboratory of Photovoltaics and Optoelectronics (LPVO) and a monitoring computer. The measurement data are automatically written to an SQL database in the monitoring computer and accessible to the users if they send queries to the database via the PVMD monitoring website. Since the Toolbox simulates the energy yield of modules with an unmodifiable layout, the solar module used for this validation study was mounted at the fixed rack as shown in Figure 4.2, in which the aforementioned module is the smaller module on the left.

Figure 4.2. The studied solar module in the PVMD monitoring system (the left one on the rack).

According to the skyline of the monitoring station, as shown in Figure 4.3 below, it is almost a free horizon except a towering chimney in the north to the rack dominating the skyline. As the measurements were taken in the month of May, the sun rose in the east-northeast, reached a maximum elevation of 56° at around 1 p.m. and set in the west-northwest, so the shading of the chimney was neglected. The shading of surrounding trees and buildings were also neglected due to their long distance to the studied module.

In order to validate the simulation results with the measurements, it is vital to recreate the realistic

Figure 4.3. The skyline taken in the PVMD monitoring station.

conditions in the Toolbox, which sets a request to accurate measurements of the weather conditions. Within the necessary inputs of the weather conditions, the Diffused Horizontal Irradiance (DHI), the Global Horizontal Irradiance (GHI), the ambient temperature and the wind speed were measured in the Weather Station and could be directly used as inputs for the Toolbox simulations. The weather measurements were taken every minute. As for the solar positions, they were calculated by the Solar Calculator developed by Earth System Research Laboratory (ESRL) in National Oceanic & Atmospheric Administration (NOAA) [40]. Based on the aforementioned irradiances and the solar positions, the Direct Normal Irradiances (DNI) were calculated with the equation

$$GHI = DNI \times cos(a_s) + DHI, \tag{4.1}$$

where a_s is the altitude of the Sun. So far, all necessary weather inputs for the Toolbox are ready. Due to the limited amount of pyranometers,the existing pyranometers in the monitoring system are used to measure the horizontal irradiance and it was not possible to directly measure the plane of array irradiance. Therefore, the validation of the weather part of the Toolbox will be done once the measurements of plane of array irradiance are available.

When the Weather Station is taking measurements of weather conditions, another two components in the station, the MPPT enclosures and PVMU, are working for the electric part of the monitoring system. The MPPT enclosures ensure that the solar modules are always producing the maximum power so that the measured outputs coincide with the values derived from the maximum power point of the I-V curves. The PVMU allows for current-voltage scanning, power supplies and communication between different components of the system. It not only provides the power output of the modules, but also records the current-voltage characteristics via I-V scanning at each time interval, which enables the comparisons between the simulated and measured I-V curves. As the measurements of the electrical parameters are taken every 5 minutes, which is longer than the one-minute interval of measurements of weather conditions, the simulations will take 5 minutes as the interval too and use the weather data at the corresponding time.

4.2. Results and Analysis

This section presents the simulation results and aims to validate the accuracy of the Toolbox by comparing the simulation results with the measurement data. The validation performed under STC

is first analysed, followed by the validation under realistic conditions. As the aim of the Toolbox is to simulate the DC power output, the analysis not only includes the validation of energy yield, but also looks into the details, including the validations of the predicted DC power as well as open-circuit voltage V_{OC} and short-circuit current I_{SC}, to determine the reasons behind the deviations.

4.2.1. Validation under Standard Test Conditions

As the DC power output is directly dependent on the current-voltage characteristics of the solar module, the final goal of the Toolbox is to recreate these characteristics and to determine the corresponding output power. In order to simulate the current-voltage characteristics, the Toolbox makes use of the electric parameters given by the manufacturers, which to be more specific are open-circuit voltage V_{OC}, short-circuit current I_{SC}, voltage at the maximum power point V_{mpp} and current at the maximum power point I_{mpp}. However, it has to be taken into account that the actual efficiency of the PV module might have degraded and differ from the efficiency given in the data sheet. Considering this, the simulation were done with electrical input parameters taken from two sources: 1) data sheet, 2) own measurements. The own measurements refer to the current-voltage curve measurements under STC performed on the solar module using LASS, as described in Section 4.1.1. For the simulations, as the module used for the validation study was connected to the MPPT and thus always worked at the maximum power point, the Toolbox used the maximum power point to predict power output too. In some other cases it might be different. For example, for the solar modules connected to the batteries, their working voltages are determined by the batteries.

The current-voltage curves given by the data sheet and the own measurements will be first compared, followed by the simulated curves based on the electrical parameters taken from these two sources. The current-voltage curves are depicted in Figure 4.4 and the corresponding parameters are tabulated in Table 4.1.

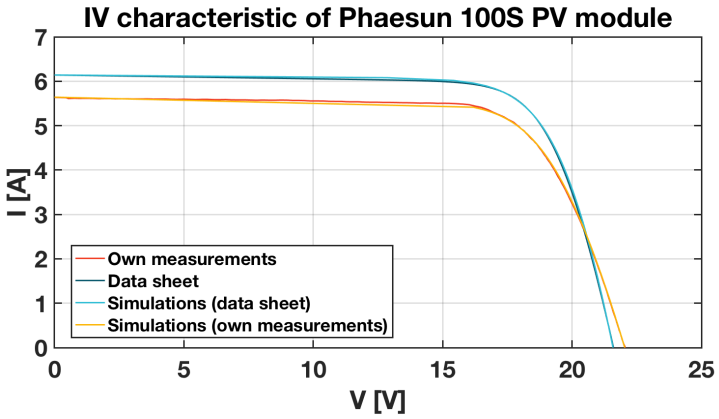

Figure 4.4. The measured and simulated I-V curves under STC.

Comparing the IV curves of own measurements to that of the data sheet, it could be concluded that in reality the module performance does not follow the current-voltage characteristics given by the manufacturers. As seen from Figure 4.4 and Table 4.1, the short-circuit current I_{SC} was lower in the own measurements compared to the rated value. This reflects the fact that its ability to generate photon current has already degraded. On the other hand, the open-circuit voltage V_{OC} was higher than it was expected. The combined effect led to a lower power output in the own measurements, which was about 10 percent less than the rated power. This is the same for simulation results. Using electric parameters given by the data sheet, the simulated power was very close to the rated power.

Table 4.1: Electric parameter measured or simulated under STC.

	V_{OC} [V]	I_{SC} [A]	V_{mpp} [V]	I_{mpp} [A]	P_{mpp} [W]	Difference [%]
Data sheet	21.6	6.14	17.6	5.68	99.97	-
Own measurements	22.06	5.64	17.34	5.20	90.08	-9.89
Simulation (data sheet)	21.58	6.14	17.49	5.71	99.90	0
Simulation (own measurements)	22.04	5.64	17.35	5.19	90.02	-9.95

On the other hand, when using electrical parameters given by the own measurements, the result deviated from the rated power by around 10 percent less, but is very close to the own measurements. According to this finding, the actual performance of this solar module has already degraded by around 10 percent. For further comparison between using electrical parameters from the data sheet and from the own measurements, the following validation under outdoor conditions will still perform simulations with electrical parameters from these two sources.

4.2.2. Validation under Realistic Conditions

When designing a photovoltaic system, the Toolbox simulates AEY based on weather conditions of the typical meteorological year (TMY), in order to predict the general output of the solar modules. However, it is not the same for the validation study. This is because the validation study cares about specific conditions and requires the actual weather data, not historical or typical weather data, as the input. Therefore, instead of using TMY weather data, it used measured weather data taken from the monitoring system. Considering the weather is changeable, the measurements were taken for a whole week (from May 7th to May 13th). The measured and simulated daily energy yields are depicted in Figure 4.5(a) and weekly energy yields are given in Figure 4.5(b).

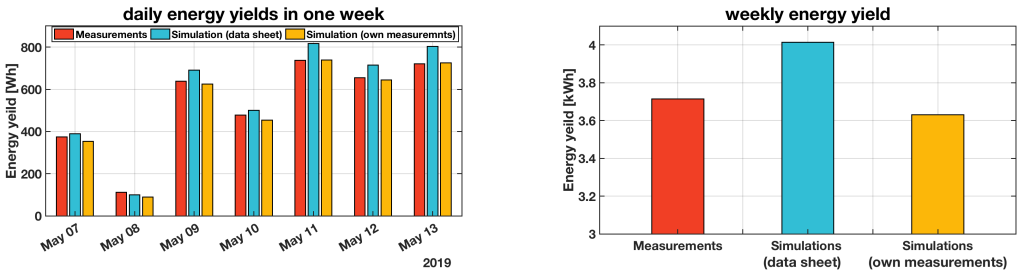

(a) Daily energy yield.

(b) Weekly energy yield.

Figure 4.5. The measured and the simulated energy yield of the studied solar module.

The measured weekly energy yield was 3.7 kWh, while the simulation based on data sheet predicted 4.0 kWh and that based on own measurements predicted 3.6 kWh. Based on Equation 4.2, the first simulation predicted 8.1 % more than actual production, while the latter simulation predicted 2.2 % less than measurements.

$$D = \frac{\sum E_{sim} - \sum E_{meas}}{\sum E_{meas}} \tag{4.2}$$

However, if the results are zoomed into each time interval, it shows that the deviation in each interval is larger than the aforementioned deviation of weekly energy yield. Figure 4.6 shows the difference of simulation results to the measurements. It could be seen from the figure that sometimes Toolbox overestimated the power (show as positive values in the figure) while sometimes underestimated instead (as the negative values). These errors cancel each other. Therefore deviations between weekly or daily yield are not a good figure of merit.

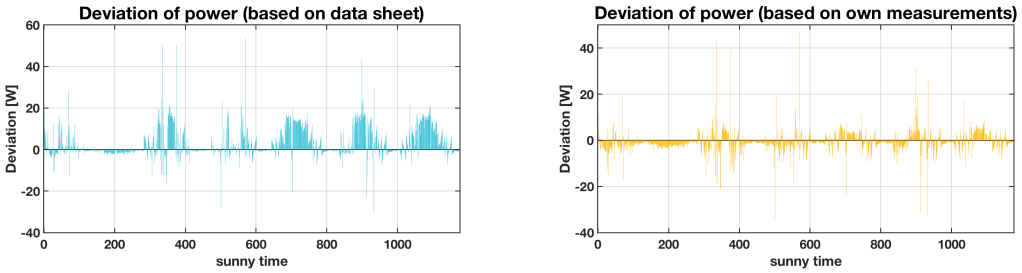

(a) Compare simulation based on data sheet.

(b) Compare simulation based on indoor measurements.

Figure 4.6. Difference between the measured and the simulated power of the studied module.

To be more precise, instead of the deviation of the weekly or daily energy yield, the deviation in each time interval was considered. As measurement data was recorded every 5 minutes, the deviation in each time interval could be referred as the 5-min deviation. These 5-min deviations actually show the error introduced by each simulation and the sum of them is the total error that the simulations produce. Therefore, a new figure of merit is put forward in this report. It compares this total error to the total production and gives a 'relative total deviation (RTD)', which can be described by

$$RTD = \frac{\sum |E_{sim,t} - E_{meas,t}|}{\sum E_{meas,t}}. \tag{4.3}$$

The variable t could be one day or one week, according to the considered time period. The results considering results in each day or in one week are given in Figure 4.7(a) and Figure 4.7(b) separately.

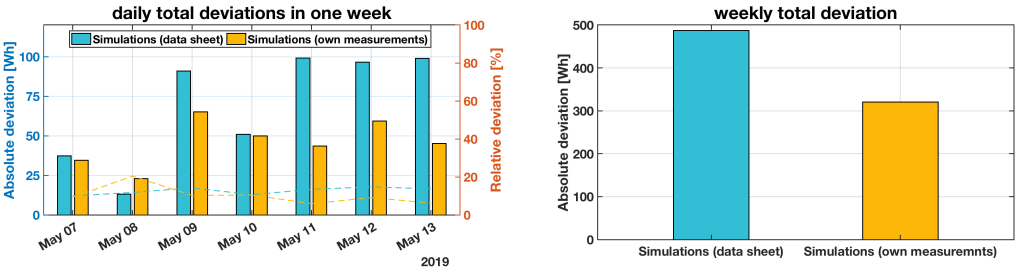

(a) Daily sum of 5-min deviation and the relative total deviation.

(b) Weekly sum of 5-min deviation.

Figure 4.7. Sum of the 5-min deviations considering period of each day or the whole week, and the relative total deviation to the energy yield.

The daily analysis shows that in different days, both simulation results deviated from the measurement data differently. The relative total deviation of each day is represented by dashed lines in the Figure 4.7(a). For both simulations, these relative total deviations fluctuated around 10 percent. In

the days less sunny, such as May 8th, even a small total deviation can result in a high relative total deviation. The weekly sum of 5-min deviations is given in Figure 4.7(b). The results show that using electrical parameters from the data sheet gave an relative total deviation of 13.1 % while using electrical parameters from the own measurements gave a lower value as 8.6 %. It can be concluded that based on the electrical inputs given by the own measurements, simulations could give a more accurate prediction in general. Therefore, it is recommended to use own measured electrical parameters, if the users want a more accurate prediction.

The analysis also zoomed into the results of each day. Here May 11th is taken as an example. The measured power output and the simulation results are depicted in Figure 4.8, followed by Figure 4.9 showing the 5-min deviations from the measurements. In this sunny day, the sun rose at 5:05 a.m., reached a maximum elevation of 56 ° at 12:40 p.m. and set at 8:15 p.m. Figure 4.8 shows that in that day, the measured output power reached a maximum value close to 100 W at noon. Dips can be found at around 9:30 a.m. and 11:30 a.m. The reason behind these dips could be explained as shading caused by the clouds. In each time interval, the 5-min deviations from the measurements were calculated for the two simulation results, of which the results are shown in Figure 4.9. As it can be seen from the figure, simulation based on own measurements had a deviation below 5 W for most of the time, except a distinct deviation of nearly 25 W found at 11:45 a.m. However, the other simulation, which is based on the data sheet, showed a much higher deviation. The largest deviation was also found at 11:45 a.m. For the rest of time, its deviation was mostly above 5 W.

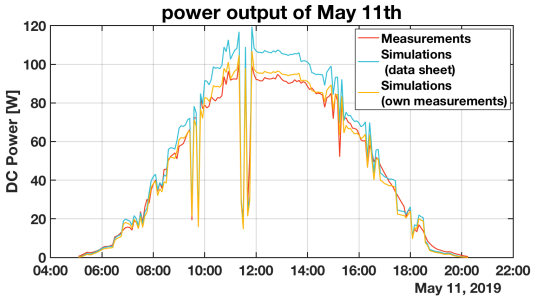

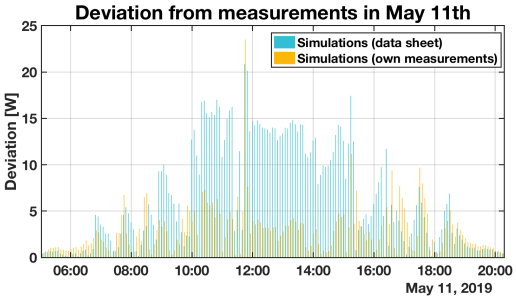

Figure 4.8. The DC power of the studied module in May 11th. **Figure 4.9.** The deviations of the simulation results in May 11th.

In order to determine the reasons behind these deviations, example comparisons between the measured and simulated I-V curves are given in Figure 4.10. Figure 4.10(a) shows the I-V curves at 10:45 a.m. At this moment, the simulation based on own measurements had the smallest deviation and the other simulation showed a relatively small deviation as well. As it can be seen from the figure, the simulated V_{OC} under both cases were close to the measurement value. The higher power predicted by the data-sheet-based simulation possibly resulted from the higher prediction of I_{SC}. As explained above, this resulted from the fact that the actual efficiency of this solar module has degraded. From this perspective, in order to simulate the I-V curves of the solar module more accurately, it would be preferred to take electrical parameters from the own measurements as the inputs.

For the moment when both simulated power had the largest deviation, which was 11:45 a.m. at that day, the I-V curves are depicted in Figure 4.10(b). It can be seen that simulation based on data sheet still predicted a higher photo current than the simulation based on own measurements predicted. However, both simulations predicted a lower photo current than the measured value. The weather data showed a global horizontal irradiance (GHI) of 343 W/m^2 at that moment. According to the linear relationship between incident irradiance and photo-generated current, this GHI should result

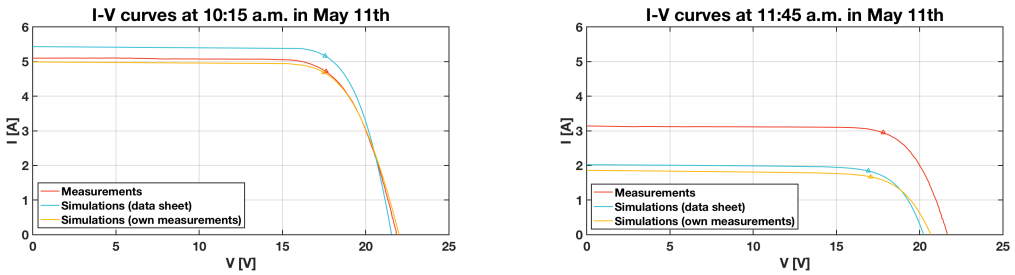

(a) At the moment with the smallest deviation.

(b) At the moment with the largest deviation.

Figure 4.10. An example comparison between measured and simulated I-V curves.

in a photo current around 1.93 A. While both the simulations predicted a photo current close to the expectation, the measurements showed a nearly 50 % higher photo current. A possible reason could be that the Toolbox does not take the reflection from the nearby buildings or trees into account. Due to the reflection, the solar module absorb more irradiance than the GHI data suggested and therefore generated this higher photo current. Therefore, representing the surrounding environment in the simulations is one of the ways to improve the accuracy of the Toolbox. By doing it, it is possible to consider the reflection from the window, the wall and the trees nearby. A model has been built to represent the surrounding environment of the PVMD station. However, due to a lack of geographical information, this model did not represent the environment perfectly. Therefore, the simulation showed a larger deviation than the aforementioned simulations did. More details about this model can be found in Appendix B.

Assuming the fill factor FF varies little under different conditions, the maximum power point(MPP) is determined by the short-circuit current I_{SC} and the open-circuit voltage V_{OC}. Therefore, it is important to accurately predict these two parameters. The measured and simulated I_{SC} and V_{OC} are shown in Figure 4.11(a) and Figure 4.11(b) respectively against time. From the outcomes several conclusions can be drawn.

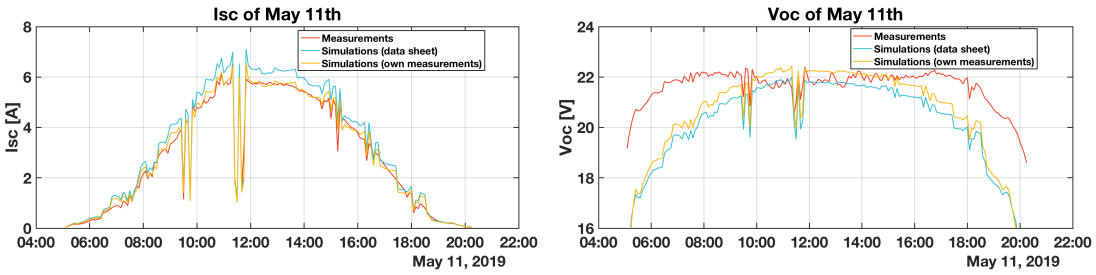

(a) Measured or simulated I_{SC}.

(b) Measured or simulated V_{OC}

Figure 4.11. Comparison of I_{SC} and V_{OC} between measurement data and simulation results.

From the comparison of I_{SC}, it can be seen that all the curves had a similar shape. The I_{SC} simulated based on the own measurements showed a good matching with the real I_{SC} for most of the time, while the I_{SC} simulated based on the data sheet always showed an obvious deviation. While the I_{SC} could increase by many times in one day, the V_{OC} varied in a smaller range. This could be explained by the logarithmic relationship between V_{OC} and I_{SC}, as described by Equation 4.4

$$V_{OC} = \frac{k_B T}{q} ln(\frac{J_{ph}}{J_0} + 1). \tag{4.4}$$

The simulated V_{OC} showed a good prediction between 10 a.m. and 4 p.m. For the own-measurements-based simulations, however, as I_{SC} was high in this time period, even a small deviation of V_{OC} could lead to a quite different power prediction. For the data-sheet-based simulations, I_{SC} showed an obvious deviation. The high and obviously-deviated I_{SC} caused a large deviation in the output power. For time before 10 a.m. and after 4 p.m., both simulations gave a good prediction of I_{SC}, but they predicted a V_{OC} distinctly deviated from the measurement data. This can explain that although simulated I_{SC} was low and close to the measurement data, the obviously-deviated V_{OC} resulted in an inaccurate prediction of output power.

In general, the simulated V_{OC} showed a worse prediction than the simulated I_{SC} did. The reason behind the deviation of V_{OC} can be explained by using constant R_S and R_{Sh}. In reality, these two electrical parameters are influenced by irradiance and temperature, which can be verified by the measurement data. Some researches[41, 42] have quantified this influence and built some correction model. They can provide some ideas to consider the varying R_S and R_{Sh} in the Toolbox. For the future version of the Toolbox, this is recommended in order to improve the accuracy of the Toolbox.

To keep the structure of the report compact, the detailed validation results of the others days in that week are not discussed here, but attached in Appendix A. Those results draw a similar conclusion as given above. It should be noted that from 3:35 p.m. to 7:30 p.m. in May 8th, the monitoring system did not note down the irradiance data but only took down the electric output, so measurements in that time period was not considered in the validation work.

4.3. Conclusions

This chapter validates the accuracy of the Toolbox with the measurement data.

Section 4.1 gives a brief introduction to experiment setups. Indoor measurements were taken in the PV Lab and outdoor measurements were performed in the PVMD monitoring station. The skyline of the monitoring station showed there was an almost free horizon so that the measured irradiance can be used as weather input data for the Toolbox directly.

Section 4.2 analysed the validation result. Measurements of I-V characteristics performed in the PV Lab showed that the actual efficiency of the studied module has already degraded. Using electrical properties given by the own measurements gave a better prediction, with an error of 8.6 %, than using electrical properties from the data sheet, with an error of 13.1 %. Therefore, to consider the degradation of solar modules, it is recommended to use own-measured electrical parameters.

5

Case Study

This chapter aims to perform energy yield predictions for tandem photovoltaic device, which is an important new feature of this version of Toolbox. It focuses on 2-terminal monolithic perovskite/c-Si tandems and consists of two case studies. First, the prediction for tandems with perovskite layers in different thicknesses is analysed in Section 5.1. These tandem devices are compared not only under STC but also under realistic conditions. Later, Section 5.2 compares the module performance between perovskite tandems and the conventional single-junction silicon technologies, focusing on their rated power under STC and their predicted AEY under real meteorological conditions. The last section, Section 5.3 draws a conclusion based on the analyses.

5.1. Energy Yield Prediction with Different Thickness of Perovskite

Of the tandem technologies, the 2-terminal monolithic tandem is taken as the default tandem cell structure in the Toolbox now. For this kind of tandem devices, it is important to match the photo currents generated in each sub cell, in order to generate a higher cell current. To realise this, a possible approach is to adjust the thicknesses of the absorber layers. This method is tested in this section, as the first case study of this chapter. Performances of perovskite/c-Si tandems with perovskite layers in different thicknesses are compared under STC as well as under realistic conditions for different locations.

5.1.1. Current Mismatching Between Sub Cells

Tandem solar cells are known to have a higher efficiency than conventional single-junction cells, since they can make a better use of photons and have a stronger absorption. Of these tandem devices, the monolithic 2-termial cells are attractive in the perspective of installation and efficiency potential[43]. However, due to the different absorption and therefore different photo currents between sub cells, the output current is limited. Considering this, when optimising the cell performance in the lab phase, the thicknesses of absorber layers are adjusted to achieve current matching. An example is given in Figure 5.1, which shows reflection, transmission and absorption under STC of a tandem solar cell with an optimised cell structure, simulated by the Cell model of Toolbox. It can be concluded from the figure that for this cell structure, applying a 420 nm-thick perovskite layer could realize the current matching, with a photo current density of 18.90 mA/cm^2 in the perovskite top cell and 18.93 mA/cm^2 in the SHJ bottom cell.

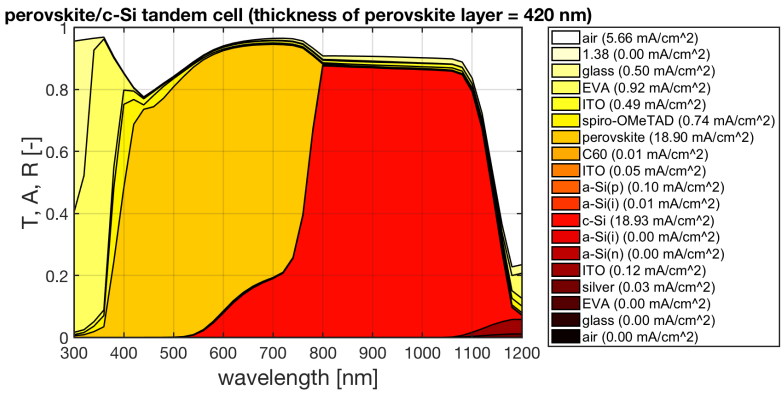

Figure 5.1. Cell absorption of a perovskite/c-Si tandem cell, with perovskite thickness equal to 420 nm.

However, realistic conditions are different from the test conditions used in the lab and also keep varying, influencing the actual efficiency of the photovoltaic devices. One of the influencing factors is the spectral variation. Since the absorber materials show a wavelength-dependent sensitivity, the spectral variation has an impact on absorbed photon fluxes and therefore the photo currents. As the sun keeps moving into different elevations during the day, this spectral variation always exists, resulting in an unavoidable current mismatching. An example is given below, where the aforementioned tandem cell was simulated based on the measured weather data of May 11th and the absorbed photon fluxes in the perovskite top and silicon heterojunction (SHJ) bottom cell are compared in Figure 5.2.

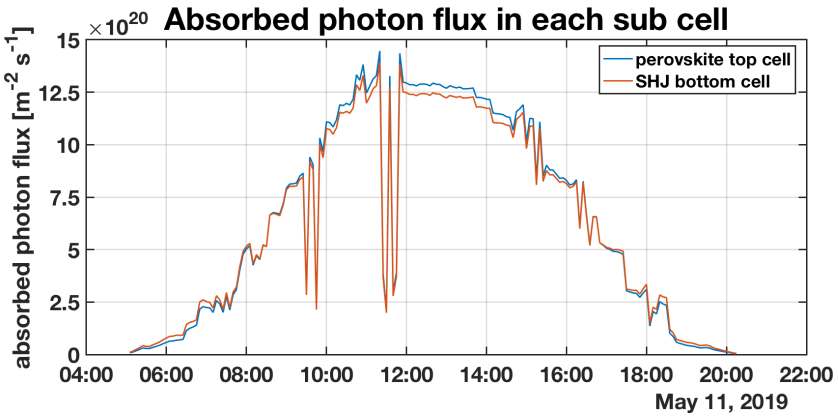

Figure 5.2. Absorbed photon flux in perovskite top and c-Si bottom cell in May 11th.

As mentioned in the validation work, this day was a sunny day except a few cloudy minutes, which can be indicated by the dips in the curves. According to the weather data, the AM1.5 spectrum was achieved twice in that day, at around 9:45 a.m. and around 3:35 p.m. Therefore, currents in the two sub cells had a best matching in these two moments. In the other time of this day, there was obvious deviation between the sub cell absorption, which could be explained as a result of spectral variation. As it is shown in Figure 2.5, when the air mass varies, or in other words when the sun is in different positions, the solar spectrum can be described by either blue-rich or blue-poor, according to the proportion of blue light. When it was before 9:45 a.m. and after 3:35 p.m., the sun was closer to the horizon, resulting in a relatively large air mass and an blue-poor spectrum. During this period, a higher proportion of photons carried red light, which travelled through the perovskite top cell and were absorbed by the SHJ bottom cell, resulting in a higher photo current in SHJ bottom

cell than in perovskite top cell. On the other hand, when it was between 9:45 a.m. and 3:35 p.m., the sun was relatively high so that solar spectra in that period were more blue-rich. Therefore, a higher proportion of photons carried blue light and were absorbed by the perovskite top cell but less of them could be absorbed by the SHJ bottom cell.

The current mismatching existing under blue-poor or blue-rich solar spectra limits the output current, but this influence could not be totally eliminated. Therefore, the perovskite thickness that gives current matching under STC is not necessarily the thickness that gives the maximum energy yield under realistic outdoor conditions with varying spectra. However, cell performances under STC are still interesting study field, from the research perspective, as novel solar technologies are studied under STC in the lab phase.

5.1.2. Performance Under STC

Perovskite/c-Si tandem cells, although they have made an impressive progress in improving their maximum power conversion efficiency, are still being developed in the lab phase. Therefore, the influence of thickness of perovskite layer on the cell performance was first analysed under STC in this case study.

The example cell used for analysis was built with optical properties, including layer material, thickness and texture, taken from literature[30]. It was a monolithic 2-terminal tandem cell, with a layer structure redrawn in Figure 5.3. This tandem device consists of, in the order that light travels through, anti-reflective coating of magnesium fluoride (MgF_2), transparent conducting layer indium tin oxide (ITO), hole transporting layer Spiro-OMeTAD, perovskite layer (with a band gap of 1.65 eV), electron transporting layer C_{60}, ITO and silicon hetero-junction (SHJ) bottom cell. The SHJ bottom cell contains a 3.5 mm-thick crystalline silicon layer, which is different from an ordinary thickness of 200 μm, to ensure that the optical path is long enough[30]. As for the perovskite layer, the thickness was varied from 390 nm to 420 nm. According to different thicknesses of perovskite layer, photo current densities generated in the perovskite top and SHJ bottom cell were simulated by the Cell model of Toolbox, and the lower current density of them was taken as the current density of the cell. The results are given in Figure 5.4.

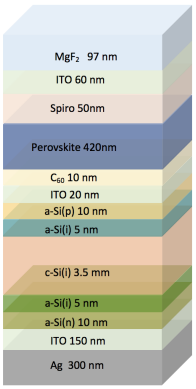

Figure 5.3. Tandem cell structure, with optical properties taken from [30].

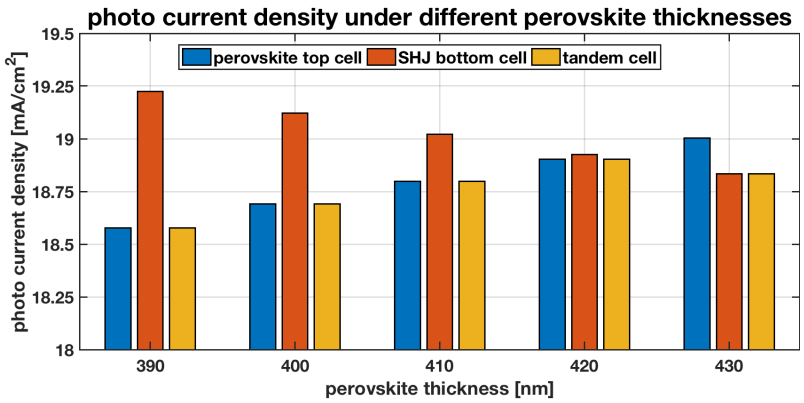

Figure 5.4. J_{ph} in sub cells and in the entire cell under different perovskite thicknesses.

It could be seen from the result that increasing the thickness of perovskite layer can have a higher current generated in the perovskite top cell but lower current in the SHJ bottom cell. For this cell

structure, the current matching was achieved at the thickness of 420 nm and so as the highest cell current density.

As for the electrical properties, except J_{ph} computed above, the other input parameters, including saturation current density J_0, series resistance R_S and shunt resistance R_{Sh}, were extracted from the published current-voltage curves [44, 45] based on the single-diode equivalent circuit model. The current-voltage characteristics of the studied tandem devices were subsequently simulated and the maximum powers under different thicknesses of perovskite layer were derived from these current-voltage curves and given in Figure 5.5. These current-voltage curves also provided electric properties inputs for the following study under realistic conditions, which requires voltage and current at the maximum power point, V_{mpp} and I_{mpp}, and open-circuit voltage V_{OC}.

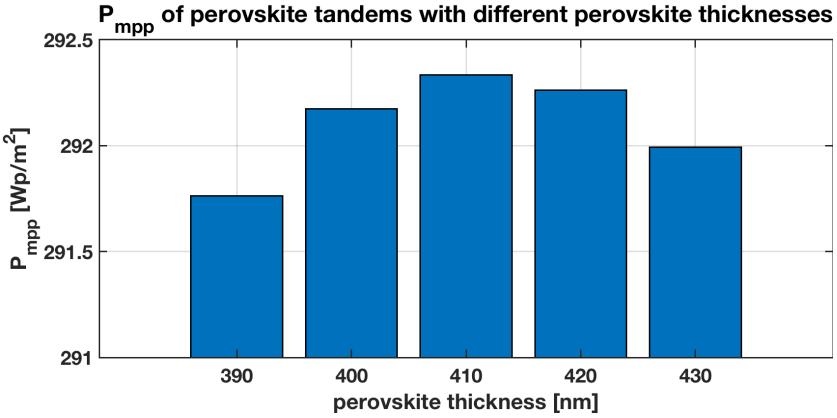

Figure 5.5. Maximum power under different thicknesses of perovskite layer.

As the outcome shows, varying the thickness of perovskite layer had an influence on the maximum power P_{mpp} that a cell could provide. The highest P_{mpp} was achieved under a thickness of 410 nm as 292.33 W_p/m^2 , while with the thickness of 420 nm, under which the best current matching was achieved, the P_{mpp} was slightly lower as 292.26 W_p/m^2. This could be analysed by the different resistances between the perovskite top cell and the SHJ bottom cell. According to the series resistance R_S and shunt resistance R_{Sh} extracted from the published current-voltage curves [44, 45], these two sub cells had quite different resistances, which resulted in different shapes of current-voltage curves between these two sub cells. When the thickness of perovskite layer increased, the current-voltage curve of perovskite top cell moved upwards while that of the SHJ bottom cell moved downwards. As a result, the current-voltage curves shifted as well and got a new maximum power point. In conclusion, the thickness which enables current matching under STC does not necessarily give the highest rated power, although the differences are small, as only 0.1 to 0.4 %.

5.1.3. Performance Under Realistic Conditions

Although solar devices, including both commercial modules and noncommercial products, are optimised under STC, their actual performance are complex and changeable in the real life as they are affected by some influencing factors, like temperature and irradiance. Therefore, the goal of the second part of case study is to perform AEY prediction under realistic conditions for the perovskite tandems. For the 2-terminal tandem devices, an important influencing factor in the real life is the spectral variation. The changing solar spectrum implies variable useful ratios of photon flux for each absorber layer, resulting in current mismatch between the sub cells. The solar spectrum is

determined by many influencing factors, such as water vapor, ozone abundance and atmospheric pollution, but here only one of the most crucial factor, air mass, is considered.

According to analysis in Section 2.2 and 5.1.1, a larger air mass refers to an blue-poor spectrum, implying a higher proportion of photons carrying low energy and available for the SHJ bottom cell, while a smaller air mass corresponds to an blue-rich spectrum, with a higher proportion of photons carrying high energy and absorbed in the perovskite top cell. Since the solar spectrum is determined by the solar position, it varies not only between different times in a day, but also in different seasons and different locations.

The influence of the spectral variation on module performance in one day has been analysed in Section 5.1.1. From the view of different seasons, if taking countries in the Northern hemisphere as an example, during summer times the sun is in higher positions than it is in the winters at the same time, resulting in blue-rich solar spectra in summer but blue-poor solar spectra in winter. Therefore, thinner perovskite layer is preferred in summer while thicker one is preferred in winter. However, it is not cost-effective for a PV array to replace solar module between seasons. A trade-off to this problem is to perform AEY prediction for that location with different thicknesses of perovskite layer and pick the optimal thickness.

Considering the spectral variation between areas with different latitudes, this optimal thickness is different between these locations. To verify this influence, in this second part of case study, AEY predictions were done for different thicknesses in different location, in order to determine optimal thicknesses for these considered locations and to compare the difference between them. These prediction were based on the weather data, including GHI, DNI, wind speed and ambient temperature taken from the Meteonorm database[32] and based on an assumption that the perovskite tandems are in the same size of commercial PV module.

Cities in three latitude areas, including Rio de Janeiro, Brazil (22.88°S, 43.28°W), Delft, the Netherlands (52.01°N, 4.36°E) and Helsinki, Finland (60.17°N, 24.94°E) were taken as examples. To compare spectral difference between these locations, their sun path diagrams were first compared as shown in Figure 5.6[46].

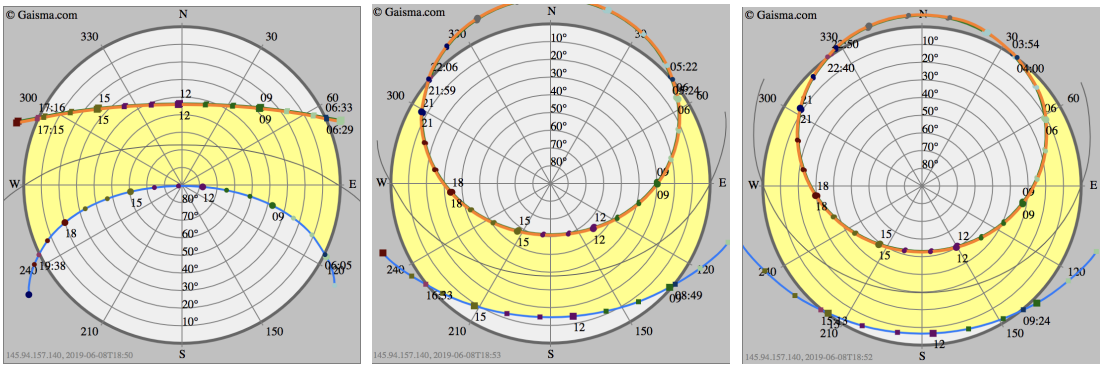

(a) Rio de Janeiro, Brazil (b) Delft, Neterlands (c) Helsinki, Finland

Figure 5.6. Sun path diagrams of studied locations[46].

The sun path diagrams indicate the sun's positions in a year. The upper orange line shows the sun path on June solstice and the lower shows the sun path on December solstice. The light-yellow area between these two lines is the annual variation of the sun path. It can be seen from the figures

that the sun mainly moves in higher elevations for low-latitude area (Rio de Janeiro) but in lower elevations for high-latitude area (Helsinki). The differences in sun positions lead to different solar spectra between these places. To quantify this influence, power-weighted average spectra of these three cities were compared.

The power-weighted average spectra were calculated based on the sun positions and GHI values taken from Meteonorm database[32]. According to the sun position, the spectral distribution of photon flux in each time interval was first calculated based on the spectra derived from SMARTS[31]. The photon flux in each wavelength interval was then divided by the total photon flux along the entire spectra (from 280 nm to 4000 nm) and expressed as the relative spectral photon flux. This relative spectra were weighted according to the contribution of GHI at that time to the annual GHI. Finally, the weighted average spectral photon fluxes of different locations were compared and shown in Figure 5.7. As a 1.65 eV perovskite layer and a 1.12 eV crystalline-silicon layer were used in this tandem cell, the limiting wavelengths for these two layers are 752 nm and 1107 nm respectively. For simplicity, the region with wavelengths below 752 nm is referred as blue light region and region with wavelengths between 752 nm and 1107 nm is referred as red light region. The percentages of spectral photon flux in blue and red light regions of different locations are tabulated in Table 5.1.

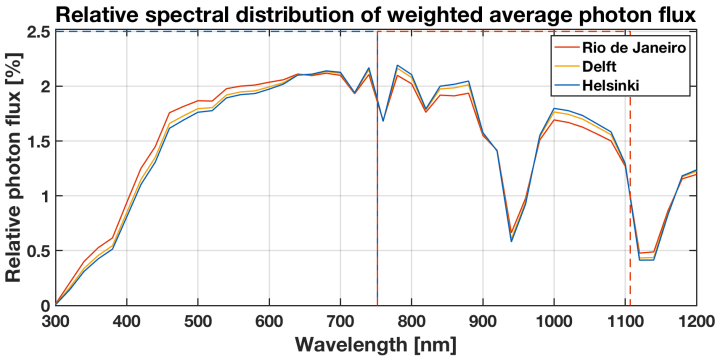

Figure 5.7. Relative spectral distributions of average photon flux weighted according to GHI, of the studied locations.

Table 5.1. Ratios of photon flux in blue light and red regions.

	Blue light (280-752 nm) [%]	Red light (752-1107 nm) [%]
Rio de Janeiro	32.98	29.38
Delft	31.94	30.05
Helsinki	31.46	30.35

According to the results, in these three cities, Rio de Janeiro has the largest percentage of blue light and Helsinki has the largest percentage of red light. It is consistent with the deduction that the Sun moves in lower elevations in a higher-latitude area, therefore this area has a relatively blue-poor average solar spectrum. Therefore, Rio de Janeiro can be regarded as a blue-rich region while Helsinki can be regarded as a blue-poor region.

After comparing the spectral difference between these locations, to see how the module performance is influenced in these blue-rich and blue-poor region and to determine whether the optimal thickness of perovskite layer is different between locations, AEY predictions of tandem devices were performed for in these area. The tandem devices had different thicknesses of perovskite layer from 390 nm to 430 nm, as they were in the analysis under UTC. As the perovskite tandems are still being developed and far away from commercialisation, there are no existing module designs can be directly used for the simulations. Therefore, as explained above, the perovskite tandems were assumed to have a normal cell width of 6 inches and cells are arranged in a 10-by-6 configuration. The module layout were same for the three locations except the tilt and azimuth angle. The tilt angles used the optimal values, which were 22°, 34° and 39° for Rio de Janeiro, Delft and Helsinki separately, taken from literature[47]. As for the azimuth angles, the module in Rio de Janeiro was facing the North while those in Delft and Helsinki were facing south. As these perovskite tandems had a

small variation in the output power, the AEYs of them did not show a large difference either. Therefore, for each location, AEYs under different thicknesses of perovskite layer were compared to the highest value among them. These relative AEYs are given in Figure 5.8.

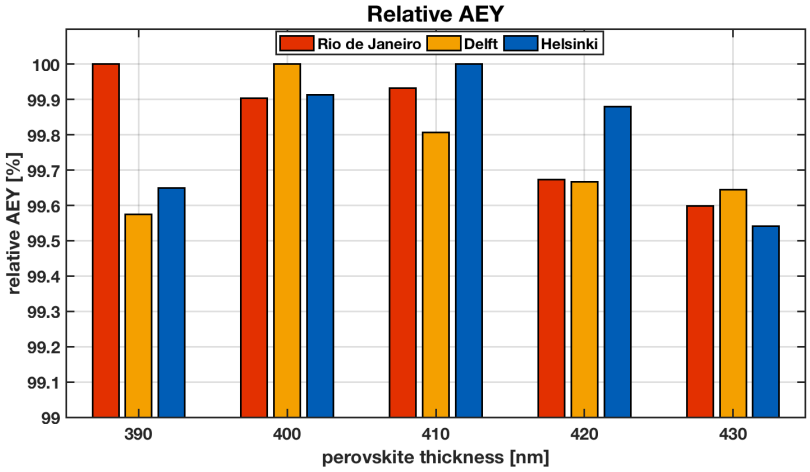

Figure 5.8. Relative AEYs compared to the highest AEY in the corresponding locations.

As it can be seen from the figure, for each location, the optimal thicknesses of perovskite layer are different. For Rio de Janeiro, the highest energy yield was found for a perovskite thickness of 390 nm, while for Delft and Helsinki these values were 400 nm and 410 nm respectively. For the low-latitude area Rio de Janeiro, as it is a blue-rich region according to the study above, the proportion of photons absorbed in the perovskite layer is the highest of these three locations. Therefore, in order to control photo current generated in the perovskite top cell and achieve current matching, perovskite tandems in Rio de Janeiro preferred a thinner perovskite layer compared to tandems in the other two locations. It is opposite for the high-latitude area Helsinki. As it is a blue-poor region, in Helsinki more incident photons carry low energy and travel through the perovskite top cell. In order to make the perovskite layer less transparent and generate a higher photo current, a thicker perovskite layer is needed. Delft is relatively blue-neutral in these three locations so that the optimal thickness is the middle value of the three optimal thicknesses. Notably, optimising perovskite thickness does not yield a noticeable AEY gain. The thickness of 390 nm, 400 nm and 410 nm gave quite similar AEY with a difference of only 0.1 %.

It should be noticed that this case study was based on some assumptions, including using electric parameters J_0, R_S and R_{Sh} derived from the published I-V curves, assuming the tandem cells have a same size as the cells in commercial modules and assuming they are stable under realistic condition. If other assumptions are made or using measured electric input parameters instead of simulated values, the results could be different. In conclusion, this case study shows an example of energy yield prediction for the new cell technology inside the Toolbox, the perovskite tandems. According to the results, users can optimise their tandem cell structure based on the simulation results given by Toolbox.

5.2. Energy Yield Prediction Between Different Cell Technologies

Although perovskite/c-Si solar cells are regarded as a promising photovoltaic technology to further increase the PCE of solar cells, they are still being developed in the lab and their actual performance

under realistic climate conditions remains unknown. Therefore, this section compares the performances between this interesting novel photovoltaic technology and conventional monofacial c-Si modules. The performances of the monofacial c-Si module and the perovskite tandem module are first compared under STC. Later, these modules are compared under realistic conditions.

5.2.1. Performance Under STC

In spite of the developing novel photovoltaic technologies, silicon solar cells still hold a market share over 90 %[48]. In this case study, a 340 Wp $N_eON^{®}2$ monofacial module from LG[49] was studied. The layout of $N_eON^{®}2$ monofacial module was also the prototype of the perovskite tandem module, as the latter module has not been commercialised yet. For the perovskite tandem module, as the following comparison under realistic conditions takes Delft as an example, according to the analysis above a tandem cell with a 400nm-thick perovskite layer was chosen. The current-voltage properties under STC are given by Figure 5.9 and details of the electrical properties are tabulated in Table 5.2.

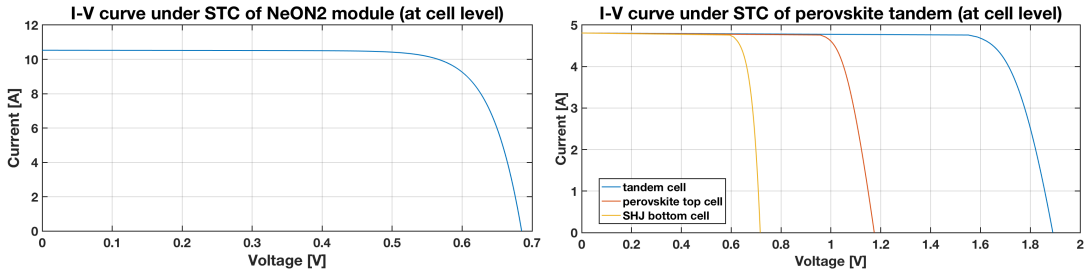

(a) $N_eON^{®}2$ monofacial module, LG[49]. (b) Perovskite/c-Si tandem module.

Figure 5.9. Current-voltage characteristics under STC of different modules (at cell level).

Table 5.2: Electrical properties of c-Si and perovskite tandem module (at module level).

	V_{OC} [V]	I_{SC} [A]	V_{mpp} [V]	I_{mpp} [A]	P_{mpp} [W]	Effiency [%]
$N_eON^{®}2$	41.1	10.53	34.5	9.86	340	19.8
Perovskite/c-Si tandem module	113.42	4.81	98.50	4.74	467	27.3

It can be seen from the results that these two kinds of cells have quite different electrical properties. As the absorbed photons are divided over the series connected top and bottom cells for this monolithic 2-terminal tandem cell, perovskite tandem gives a short-circuit current I_{SC} as only 4.81 A. This I_{SC} is more than two-times lower than that of the c-Si module, which is 10.53 A. On the other hand, the perovskite tandem gives a much larger open-circuit voltage V_{OC} as 113.42 V, compared to 41.1 V of the c-Si module. This is because the series connection between the sub cells and perovskite has a larger V_{OC} than c-Si has. The combined effect makes perovskite tandem module has a P_{mpp} as 467 W and an efficiency of 27.3 %, while those of c-Si module are 340 W and 19.8 %.

5.2.2. Performance Under Realistic Conditions

Although the perovskite tandems have an obviously higher efficiency than the conventional c-Si modules under STC, in reality, their module performances are influenced by the real working con-

ditions. To compare their performances in the real life, the AEYs of these modules were compared. They were assumed to be in the same place in Delft, with a same arrangement as the tandem devices were put in Delft in the first case study. Considering that these modules have different rated power, it is not fair to compare their performances just based on the respective of AEYs. To solve this problem, their specific yields are also compared. The results are represented in Figure 5.10.

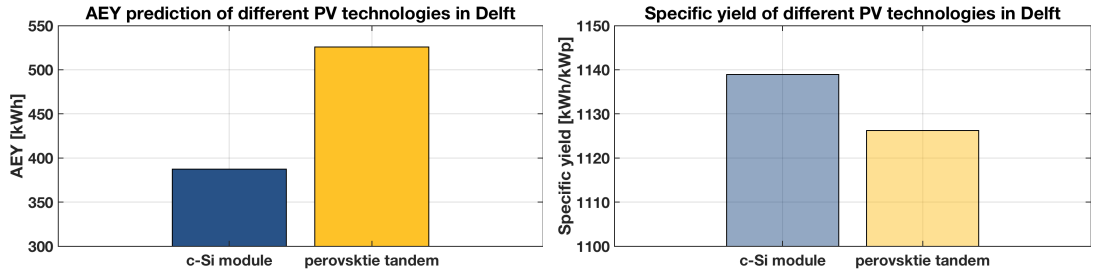

(a) AEY predictions of different PV technologies. (b) Specific yields of different PV technologies

Figure 5.10. Comparison of AEY and specific yield between c-Si and perovskite tandem module.

The result shows that, under the same meteorological conditions, perovskite tandem module gave a higher AEY as 526 kWh, while c-Si module only produced 387 kWh. The reason, as mentioned above, is that the studied perovskite tandem module has a larger rated power than c-Si module has. Therefore, besides AEY, the specific yields are also compared here. Specific yield is the AEY generated by each kWp installed, described as

$$\text{Specific yield} = \frac{\text{AEY}}{\text{P}_0}\,[\text{kWh/kWp}]. \tag{5.1}$$

According to the computation, perovskite tandem gave a specific yield of 1126 kWh/kWp, while that of c-Si module was higher as 1139 kWh/kWp. The result infers that under real working conditions, perovskite tandem is more sensitive to the meteorological conditions, especially the spectral changes.

5.3. Conclusions

This chapter performed case studies for the new available cell technology included in the Toolbox, the perovskite/c-Si tandem solar cells. It analyses the influence of the thickness of perovskite layer and compares the module performances between this novel PV technology and conventional technologies.

Section 5.1 focuses on the impact of perovskite thickness. It can be concluded that for the reference tandem configuration, at a perovskite thickness of 420 nm, the photo current generated in the perovskite top and c-Si bottom cell reach a good matching. However, this thickness not necessarily give the highest rated power. The thickness with the highest rated power is slighter smaller, as 410 nm. This section also shows that the low-latitude city, Rio de Janeiro, has a blue-rich solar spectrum in general, while the high-latitude city, Helsinki, has a relatively blue-poor spectrum. Due to the spectral variation, the optimal perovskite thickness that gives the highest AEY is different between locations. It is 390 nm, 400 nm and 410 nm for Rio de Janeiro, Delft and Helsinki respectively. The AEY could be improved by up to 0.4 % via improving the perovsktie thickness.

Section 5.2 compares the module performance between the tandem cell and conventional monofacial silicon modules. According to the result, the perovskite tandem module had a higher rated power and rated efficiency. Under realistic conditions, it had a higher AEY as well, but its specific yield is lower than that of the silicon module. Therefore, it can be inferred from the results that the 2-terminal monolithic tandem cell is sensitive to spectral variations in the real life, especially the spectral changes.

6

Conclusions and Recommendations

This chapter summarises conclusions drawn from the work presented in this MSc project and gives recommendations for the future study. In this project, a DC energy yield prediction model for photovoltaic systems, called the PVMD Toolbox, is developed. The Toolbox has been built by *Elias Garcia Goma* and optimised by *Julen Garro Etxebarria* in the PVMD group, and version 3 of the Toolbox is finished in this MSc project. The goal of this project is to perform

Improvements and experimental validation of a PV system performance prediction model – the PVMD Toolbox.

To achieve this goal, several sub goals were set, of which the results are described in Section 6.1. Later, based on the current work, recommendations for the future study are given in Section 6.2.

6.1. Conclusions

The sub goals to answer the research question are improvements, experimental validation and case studies. This section answers these sub goals.

6.1.1. Improvements of the Toolbox

This version of Toolbox is improved in two aspects: adding new features as well as improving the accuracy. These improvements are described in Chapter 2 and 3, regarding the work performed on the Optical Model and on the Thermal and Electric Model respectively.

Chapter 2 shows improvements on the Optical Model. These improvements breaks the limitations of the Optical Model in version 2, which are mentioned in Section 1.3.2.

Section 2.1 solves the problem of expanding the scope of application. This version of Toolbox can simulate the performance of tandem devices, of which the perovskite/c-Si tandem devices is taken as the representative. Users are also free to define their own cell structure following the examples given by the Toolbox. The refractive indices of most commonly-used material are included. Users only need to define the layer material, thickness and roughness.

Section 2.2 focuses on considering the influence of realistic solar spectra. The section simulates solar spectra by using SMARTS 2.9.5[31] and shows that the solar spectrum varies with different AMs. These spectra are included in the Toolbox to give an accurate prediction of absorbed irradiance and

photon flux.

Lastly, Section 2.3 describes the modification of individual cell analysis. The Toolbox now simulates individual cell absorption to consider different performances between cells. To realise the individual analysis, an auxiliary tool is added to give suggestion on the rays used in the ray tracing process.

Chapter 3 describes improvements on the Thermal and Electric Models. Some of the modifications were carried out to make the Toolbox compatible with tandem devices and the others were carried out to improve the accuracy.

Section 3.1 describes corrections to the Thermal Model, including adjusting the ratio of glass absorption to the total absorption from 5 % to 1.4 %. Some mistakes in the formulas are corrected as well. In addition, users can choose whether to calculate individual cell temperature or average temperature.

Section 3.2 details modifications in the Electric Model. First, a new method to calculate temperature dependence of V_{OC} and I_{SC} is added to the Toolbox. It calculates the coefficients based on the temperature dependence of the band gap energy, which is $\frac{dE_g}{dT} = -2.3 \times 10^{-4} eV/K$ for c-Si cells[36] and $\frac{dE_g}{dT} = -5.2 \times 10^{-4} eV/K$ for PMMA/($CH_3NH_3PbI_3$), derived from the results by [23]. Besides, the Electric Model has been modified to compute photo current I_{ph} based on the absorbed photon flux density and simulate I-V curve for each cell.

6.1.2. Validation of the Toolbox

In Chapter 4, the accuracy of the Toolbox has been validated. Section 4.1 introduces that indoor measurements were performed in the PV Lab and outdoor measurements were done in the PVMD monitoring station. Validation results are detailed in Section 4.2.

The studied solar module was first tested under STC in the PV Lab. The indoor measurements showed that the actual efficiency of this module has already degraded by around 10 %. Later, validation with outdoor measurements was performed. A new figure of merit is put forward here, which is called 'relative total deviation' and calculates the relation between the sum of deviations to total energy yield. From the validation results, if the Toolbox use electrical parameter given by the data sheet, it cannot consider the degradation of solar modules. This introduces a relative total deviation around 13.1 %. To consider the degradation, it is recommended to use own-measured electrical parameters, in which case the relative total deviation is reduced to 8.6 %.

6.1.3. Case studies of the Toolbox

In Chapter 5, case studies are carried out for the tandem devices, where tandems are assumed to have a same size as a 60-cell commercial solar module.

Section 5.1 shows that the perovskite thickness has an influence on the current matching and cell efficiency. For the reference tandem configuration, a perovskite thickness of 420 nm gives the best current matching, but a thickness of 410 nm gives the highest rated power. Under realistic weather conditions, the perovskite thickness giving the highest AEY is 390 nm, 400 nm and 410 nm for Rio de Janeiro (a low-latitude area), Delft (a mid-latitude area) and Helsinki (a high-latitude area) respec-

tively. It was found that AEY of perovskite tandems can be improved up to 0.4 % by optimising the perovskite thickness.

Section 5.2 compares the module performance between tandem devices and conventional silicon modules. Under STC, the perovskite tandem had a higher output power and a higher module efficiency, which in this case is 467 Wp and 27.3 % for perovskite tandem and 340 Wp and 19.8 % for c-Si module. Under realistic conditions, perovskite tandem module also gives a higher AEY as 526 kWh compared to 387 kWh of c-Si module. However, the specific yield of perovskite is lower as 1126 kWh/kWp, while c-Si gives 1139 kWh/kWp. Therefore, it can be inferred that perovskite tandems are more sensitive to the spectral variation.

6.2. Recommendations

Although the Toolbox has been improved and validated with the measurements, in order to further improve its accuracy, some work are suggested for the future study, including:

- Taking irradiance and temperature dependence of series resistance R_S and shunt resistance R_{Sh} into consideration. Toolbox now takes these parameters constant, however, according to the data given by the PVMD monitoring system, these two parameter vary with time. The relation of R_S and R_{Sh} with irradiance and temperature have been analysed by some researchers, such as Eikelboom and Reinders [41] and Xiao et al[42]. Xiao also provides an adaptive parameter model. Including irradiance and temperature dependence of R_S and R_{Sh} in the simulations could be a possible way to improve the accuracy.

- Including complicated cell arrangements. This version of Toolbox defaults to the cell configuration with all cells wired in series. However, some solar modules, such as modules with half-size cells, use series-parallel circuits, requiring a flexible model to compute module current and voltage from the cell level. In addition, for the tandem devices, only 2-terminal monolithic devices are possible to analyse in the Toolbox. Since 3-terminal and 4-terminal tandem cells are also interesting fields of study and are predicted to have high efficiency and better stability, they should be included in the Toolbox as well.

- Further validation for the Optical and Thermal Models. Due to the lack of equipment, the module temperature and irradiance on the plane of array were not able to measure. Toolbox showed a 8.6 % deviation from the measurement data and its deviation was only possible to be analysed from the perspective of electric properties. Validations of the Optical and Thermal Models could enable a deeper research to find out other possible reasons and to further increase the accuracy.

- Providing users with instructions of the Toolbox. This version of Toolbox has already been tested in some other projects within the PVMD group. According to the users' experience, a limitation of Toolbox is that it takes users some time to fully understand the Toolbox and to customise some simulation settings. Therefore, an user instruction is needed to help users get familiar with the Toolbox quicker and better.

A

Validation Results

The validation results are detailed in this appendix. Simulations were done with electrical parameters given by: (1) data sheet; (2) own measurements. Measured and simulated output power are given. The deviations of simulation results to the measurements are also given.

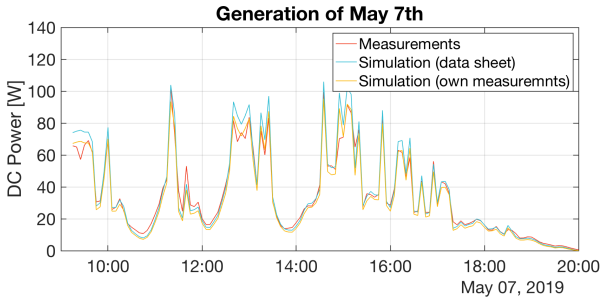

Figure A.1. The measured or simulated power in May 7th.

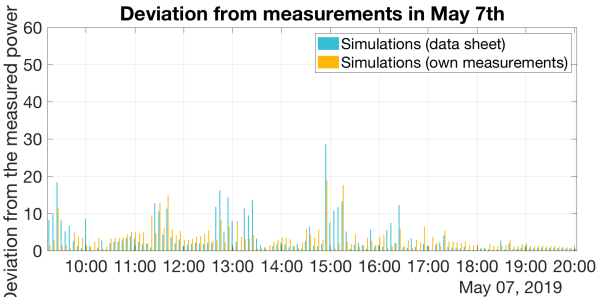

Figure A.2. The deviations of simulation results in May 7th.

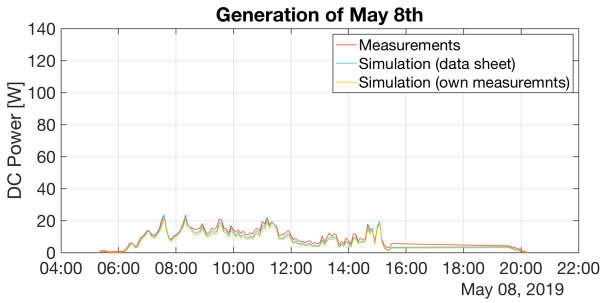

Figure A.3. The measured or simulated power in May 8th.

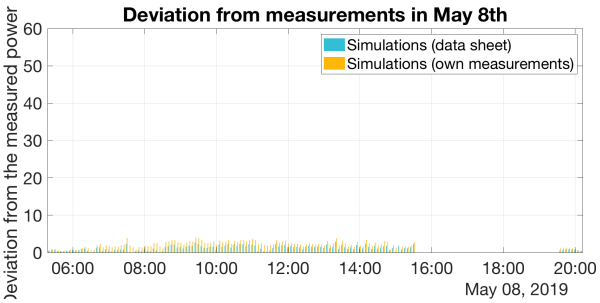

Figure A.4. The deviations of simulation results in May 8th.

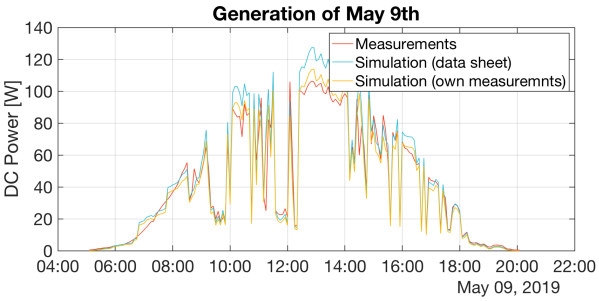

Figure A.5. The measured or simulated power in May 9th.

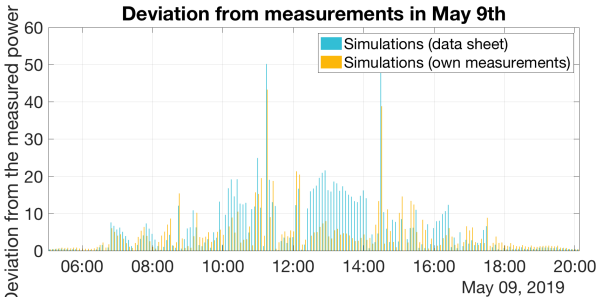

Figure A.6. The deviations of simulation results in May 9th.

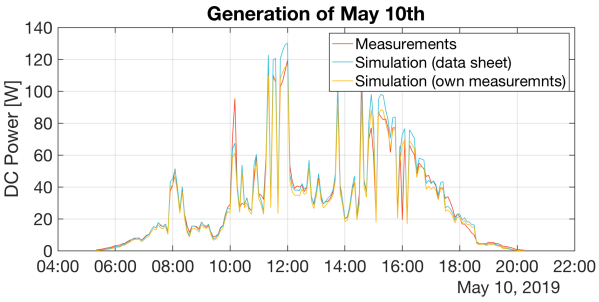

Figure A.7. The measured or simulated power in May 10th.

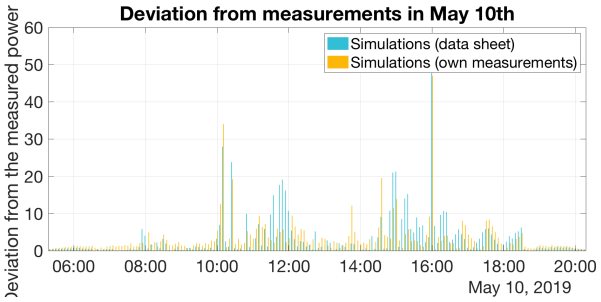

Figure A.8. The deviations of simulation results in May 10th.

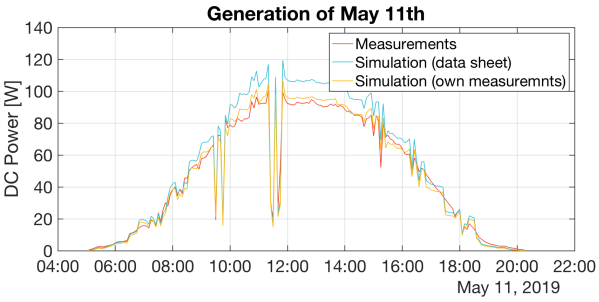

Figure A.9. The measured or simulated power in May 11th.

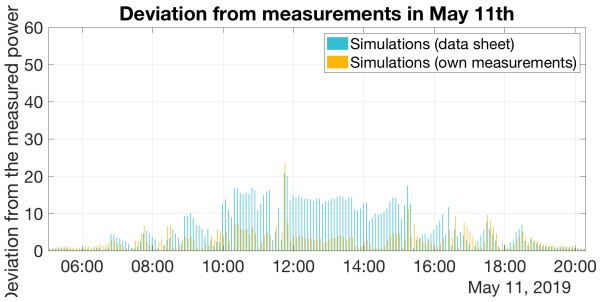

Figure A.10. The deviations of simulation results in May 11th.

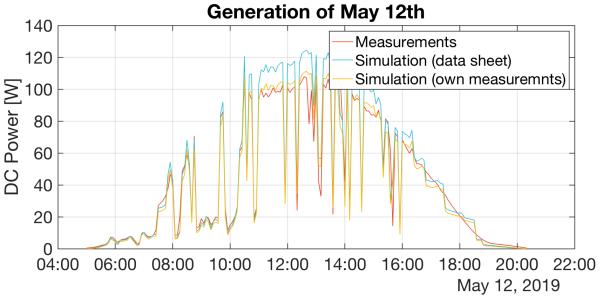

Figure A.11. The measured or simulated power in May 12th.

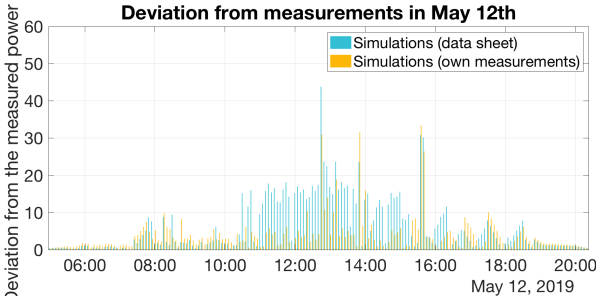

Figure A.12. The deviations of simulation results in May 12th.

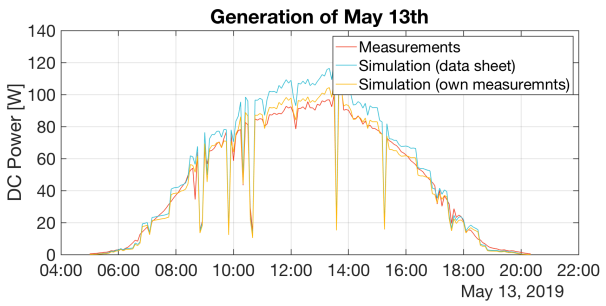

Figure A.13. The measured or simulated power in May 13th.

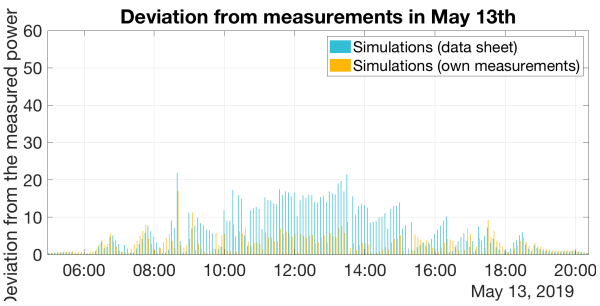

Figure A.14. The deviations of simulation results in May 13th.

B

Module Geometries Considered in the Validation Work

The validation results discussed this thesis report used the module geometry given in Figure B.1(a), resulting in a sensitivity map as Figure B.2(a). This model assumed a free horizon and did not consider reflection from the window, the wall and the trees nearby. A 3-D model considering the real surroundings of the PVMD monitoring station was built as well, as given in Figure B.1(b). This model gave a sensitivity as Figure B.2(b) shows. Due to a lack of geographical information, this model did not perfectly represent the surrounding environment, thus gave a bad prediction. However, if users have the geographical data, they can build a 3-D model like this, in order to consider shading and reflection caused by the surrounding buildings and trees.

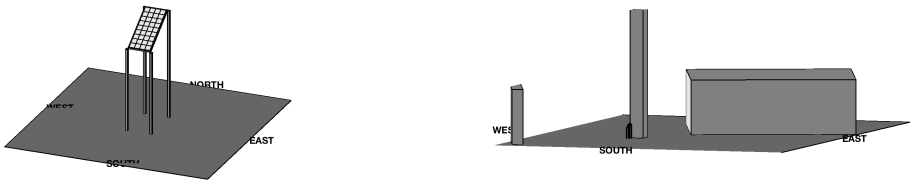

(a) 3-D model of the studied module.

(b) 3-D model of the PVMD monitoring station.

Figure B.1. Module geometry involved in the validation work.

(a) Considering only module.

(b) Considering the environment.

Figure B.2. Sensitivity maps involved in the validation work.

Bibliography

[1] Girish Kumar Singh. Solar power generation by pv (photovoltaic) technology: A review. *Energy*, 53:1–13, 2013.

[2] Russell S Ohl. Light-sensitive electric device, June 25 1946. US Patent 2,402,662.

[3] Russell S Ohl. Light-sensitive electric device including silicon, June 15 1948. US Patent 2,443,542.

[4] Kunta Yoshikawa, Hayato Kawasaki, Wataru Yoshida, Toru Irie, Katsunori Konishi, Kunihiro Nakano, Toshihiko Uto, Daisuke Adachi, Masanori Kanematsu, Hisashi Uzu, et al. Silicon heterojunction solar cell with interdigitated back contacts for a photoconversion efficiency over 26%. *Nature Energy*, 2(5):17032, 2017.

[5] SolarPower Europe. Global market outlook for solar power 2019 - 2023, 2019.

[6] PVSyst. PVSyst software, 2018.

[7] CP Kandasamy, P Prabu, and K Niruba. Solar potential assessment using pvsyst software. In *Green Computing, Communication and Conservation of Energy (ICGCE), 2013 International Conference on*, pages 667–672. IEEE, 2013.

[8] NREL. System advisor model (sam), 2018.

[9] Nate Blair, Aron P Dobos, Janine Freeman, Ty Neises, Michael Wagner, Tom Ferguson, Paul Gilman, and Steven Janzou. System advisor model, sam 2014.1. 14: General description. 2014.

[10] HOMER Energy. Homer - hybrid renewable and distributed generation system design software, 2018.

[11] ECN part of TNO. Enhanced energy yield and novel applications with double-sided (bifacial) pv, 2018.

[12] IMEC. Imec and energyville present unique simulation framework to accurately determine energy yield of bifacial solar modules and systems, 2019.

[13] William Shockley and Hans J. Queisser. Detailed balance limit of efficiency of p-n junction solar cells. *Journal of Applied Physics*, 32(3):510–519, 1961.

[14] Constantinos C. Stoumpos and Mercouri G. Kanatzidis. Halide perovskites: Poor man's high-performance semiconductors. *Advanced Materials*, 28(28):5778–5793.

[15] Akihiro Kojima, Kenjiro Teshima, Yasuo Shirai, and Tsutomu Miyasaka. Organometal halide perovskites as visible-light sensitizers for photovoltaic cells. *Journal of the American Chemical Society*, 131(17):6050–6051, 2009. PMID: 19366264.

[16] National Renewable Energy Laboratory. Best research-cell efficiencies, 2018.

[17] Weijun Ke, Constantinos C Stoumpos, and Mercouri G Kanatzidis. "unleaded" perovskites: Status quo and future prospects of tin-based perovskite solar cells. *Advanced Materials*, page 1803230, 2018.

[18] Weijun Ke and Mercouri G Kanatzidis. Prospects for low-toxicity lead-free perovskite solar cells. *Nature communications*, 10(1):965, 2019.

[19] Efat Jokar, Cheng-Hsun Chien, Cheng-Min Tsai, Amir Fathi, and Eric Wei-Guang Diau. Robust tin-based perovskite solar cells with hybrid organic cations to attain efficiency approaching 10%. *Advanced Materials*, 31(2):1804835, 2019.

[20] Wei Chen, Yongzhen Wu, Youfeng Yue, Jian Liu, Wenjun Zhang, Xudong Yang, Han Chen, Enbing Bi, Islam Ashraful, Michael Grätzel, and Liyuan Han. Efficient and stable large-area perovskite solar cells with inorganic charge extraction layers. 350(6263):944–948, 2015.

[21] Moritz H Futscher and Bruno Ehrler. Efficiency limit of perovskite/si tandem solar cells. *ACS Energy Letters*, 1(4):863–868, 2016.

[22] Oxford PV. Oxford pv perovskite solar cell achieves 28% efficiency, 2018.

[23] Thomas Dittrich, Celline Awino, Pongthep Prajongtat, Bernd Rech, and Martha Ch Lux-Steiner. Temperature dependence of the band gap of ch3nh3pbi3 stabilized with pmma: a modulated surface photovoltage study. *The Journal of Physical Chemistry C*, 119(42):23968–23972, 2015.

[24] Giles E Eperon, Maximilian T Hörantner, and Henry J Snaith. Metal halide perovskite tandem and multiple-junction photovoltaics. *Nature Reviews Chemistry*, 1(12):0095, 2017.

[25] Moritz H Futscher and Bruno Ehrler. Modeling the performance limitations and prospects of perovskite/si tandem solar cells under realistic operating conditions. *ACS Energy Letters*, 2(9):2089–2095, 2017.

[26] Elias Garcia Goma. Development of Cell to System Annual Energy Yield Toolbox for Bifacial Modules. Master's thesis, Delft University of Technology, the Netherlands, 2018.

[27] Rudi Santbergen, Tomomi Meguro, Takashi Suezaki, Gensuke Koizumi, Kenji Yamamoto, and Miro Zeman. Genpro4 optical model for solar cell simulation and its application to multijunction solar cells. *IEEE Journal of Photovoltaics*, 7(3):919–926, 2017.

[28] R Santbergen, VA Muthukumar, RME Valckenborg, WJA van de Wall, AHM Smets, and M Zeman. Calculation of irradiance distribution on pv modules by combining sky and sensitivity maps. *Solar Energy*, 150:49–54, 2017.

[29] A. Smets, K. Jäger, O. Isabella, M. Zeman, and R. van Swaaij. *Solar Energy: The Physics and Engineering of Photovoltaic Conversion, Technologies and Systems*. UIT Cambridge, 2016.

[30] Maximilian T Hörantner and Henry J Snaith. Predicting and optimising the energy yield of perovskite-on-silicon tandem solar cells under real world conditions. *Energy & Environmental Science*, 10(9):1983–1993, 2017.

[31] NREL. Smarts: Simple model of the atmospheric radiative transfer of sunshine, 2018.

[32] Genossenschaft METEOTEST. Meteonorm version 7.3.2, 2019.

[33] Gerry Julian Faturrochman. Design Optimization of Bifacial Photovoltaic Noise Barriers Using a High Granularity Energy Yield Modelling Approach. Master's thesis, Delft University of Technology, the Netherlands, 2017.

[34] Gilles Notton, Christian Cristofari, Michel Mattei, and Philippe Poggi. Modelling of a double-glass photovoltaic module using finite differences. *Applied Thermal Engineering*, 25(17-18):2854–2877, 2005.

[35] E Klugmann and E Radziemska. Alternative sources of energy. *PV Energetic*, 1999.

[36] Hellmuth F Wolf. Semiconductors. 1971.

[37] E Radziemska and Eugeniusz Klugmann. Thermally affected parameters of the current–voltage characteristics of silicon photocell. *Energy Conversion and Management*, 43(14):1889–1900, 2002.

[38] Noriko Onoda-Yamamuro, Takasuke Matsuo, and Hiroshi Suga. Calorimetric and ir spectroscopic studies of phase transitions in methylammonium trihalogenoplumbates (ii). *Journal of Physics and Chemistry of Solids*, 51(12):1383–1395, 1990.

[39] Hong-Hua Fang, Raissa Raissa, Mustapha Abdu-Aguye, Sampson Adjokatse, Graeme R Blake, Jacky Even, and Maria Antonietta Loi. Photophysics of organic–inorganic hybrid lead iodide perovskite single crystals. *Advanced Functional Materials*, 25(16):2378–2385, 2015.

[40] NOAA. Noaa solar calculator. `http://https://www.esrl.noaa.gov/gmd/grad/solcalc/calcdetails.html`. Accessed: 2019-05-30.

[41] JA Eikelboom and A Reinders. Determination of the irradiation dependent efficiency of multicrystalline si pv modules on basis of iv curve fitting and its influence on the annual performance. *Measurement*, 1:3, 01 1997.

[42] Weidong Xiao, W. G. Dunford, and A. Capel. A novel modeling method for photovoltaic cells. In *2004 IEEE 35th Annual Power Electronics Specialists Conference (IEEE Cat. No.04CH37551)*, volume 3, pages 1950–1956 Vol.3, June 2004.

[43] Jérémie Werner, Bjoern Niesen, and Christophe Ballif. Perovskite/silicon tandem solar cells: Marriage of convenience or true love story? – an overview. *Advanced Materials Interfaces*, 5(1):1700731.

[44] Michael Saliba, Taisuke Matsui, Konrad Domanski, Ji-Youn Seo, Amita Ummadisingu, Shaik M Zakeeruddin, Juan-Pablo Correa-Baena, Wolfgang R Tress, Antonio Abate, Anders Hagfeldt, et al. Incorporation of rubidium cations into perovskite solar cells improves photovoltaic performance. *Science*, 354(6309):206–209, 2016.

[45] Keiichiro Masuko, Masato Shigematsu, Taiki Hashiguchi, Daisuke Fujishima, Motohide Kai, Naoki Yoshimura, Tsutomu Yamaguchi, Yoshinari Ichihashi, Takahiro Mishima, Naoteru Matsubara, et al. Achievement of more than 25% conversion efficiency with crystalline silicon heterojunction solar cell. *IEEE Journal of Photovoltaics*, 4(6):1433–1435, 2014.

[46] GAISMA. Sunrise, sunset, dawn and dusk times around the world!, 2019.

[47] Mark Z Jacobson and Vijaysinh Jadhav. World estimates of pv optimal tilt angles and ratios of sunlight incident upon tilted and tracked pv panels relative to horizontal panels. *Solar Energy*, 169:55–66, 2018.

[48] Mehul C Raval and Sukumar Madugula Reddy. Industrial silicon solar cells. In *Solar Cells*. IntechOpen, 2019.

[49] LG Electronics Inc. LG solar., 2019.